Comparative Study of Active Flow Control Strategies for Lift Enhancement of a Simplified High-Lift Configuration

Veer N. Vatsa[*]

NASA Langley Research Center, Hampton,VA 23681

Benjamin Duda[†]

Dassault Systemes, Landshuter Allee 8, 80637 Munich, Germany

John C. Lin [‡], Latunia P. Melton[§], David P. Lockard[¶], Matthew O'Connell[‖], and Judith A. Hannon[**]

NASA Langley Research Center, Hampton,VA 23681

Numerical simulations have been performed for a simplified high-lift (SHL) version of the Common Research Model (CRM) configuration, where the Fowler flaps of the conventional high-lift (CRM-HL) configuration are replaced by a set of simple hinged flaps. These hinged flaps are equipped with integrated modular active flow control (AFC) cartridges on the suction surface, and the resulting geometry is known as the CRM-SHL-AFC configuration. The main objective is to make use of AFC devices on the CRM-SHL-AFC configuration to recover the aerodynamic performance (lift) of the CRM-HL configuration. In the current paper, a Lattice Boltzmann method-based computational fluid dynamics (CFD) code, known as PowerFLOW® is used to simulate the entire flow field associated with the CRM-SHL-AFC configuration equipped with several different types of AFC devices. The transonic version of the PowerFLOW® code that has been validated for high speed flows is used to accurately simulate the flow field generated by the high-momentum actuators required to mitigate reversed flow regions on the suction surfaces of the main wing and the flap. The numerical solutions predict the expected trends in aerodynamic forces as the actuation levels are increased. More efficient AFC systems and actuator arrangements emerged based on the parametric studies performed prior to a Fall 2018 wind tunnel test. Preliminary comparisons of the numerical solutions for lift and surface pressures are presented here with the experimental data, demonstrating the usefulness of CFD for predicting the flow field and lift characteristics of AFC-enabled high-lift configurations.

[*]Senior Research Scientist, Computational AeroSciences Branch, Research Directorate; Associate Fellow AIAA

[†]Senior Technical Specialist, Simulia Aerospace & Defense

[‡]Senior Research Scientist, Flow Physics Branch, Research Directorate; Associate Fellow AIAA

[§]Senior Research Scientist, Flow Physics Branch, Research Directorate; Associate Fellow AIAA

[¶]Senior Research Scientist, Computational AeroSciences Branch, Research Directorate; Senior Member AIAA

[‖]Research Scientist, Computational AeroSciences Branch, Research Directorate; Member AIAA

[**]Senior Research Scientist, Flow Physics Branch, Research Directorate

Nomenclature

C_L	lift coefficient, $F_z/(0.5\rho_\infty V_\infty{}^2 S)$
C_p	pressure coefficient, $(p - p_\infty)/(0.5\rho_\infty V_\infty{}^2)$
c	chord
F_z	z-component of integrated force
M	Mach number
$\dot{m}$	total mass flow rate through actuators
p	static pressure
Re	Reynolds number based on mean aerodynamic chord
S	wing reference area
V	total velocity
3-D	three-dimensional
x, y, z	Cartesian coordinates
y^+	turbulence length scale
α	angle of attack
η	normalized semispan location
ρ	density

Subscripts:

t	total quantity
∞	freestream quantity

Abbreviations:

AFC	active flow control
CFD	computational fluid dynamics
CRM	Common Research Model
DNS	direct numerical simulation
HL	high lift
IB	inboard
LaRC	Langley Research Center
LBM	Lattice Boltzmann Method
MAC	mean aerodynamic chord
NASA	National Aeronautics and Space Administration
NPR	nozzle pressure ratio
OB	outboard
SHL	simplified high lift
VLES	very large eddy simulation
VR	variable resolution

I. Introduction

The high-lift systems of modern transport aircraft strongly influence the sizing, economics, and safety of the aircraft design [1]. The NASA Advanced Air Transport Technology (AATT) Project is seeking to demonstrate the potential benefits of reducing the cruise drag (and therefore fuel burn) associated with modern high-lift systems without sacrificing aerodynamic and acoustic performance during takeoff and landing operations. One possible approach is to use active flow control (AFC) [2, 3] to provide the required low-speed lift performance while reducing the cruise drag associated with the external mechanisms used to deploy a conventional slotted flap (Fowler flap) during high-lift operations [4, 5].

A recent system integration study by Hartwich et al. [5, 6] indicated that up to a 2.25% fuel burn reduction is possible if an AFC-enabled simplified high-lift system (i.e., simple hinged flaps inboard and outboard) could provide the necessary lift at the approach angle of attack. The AFC-related performance gains are primarily due to the 3.3-count excrescence drag reduction from the removal of the external fairings for the Fowler flap mechanism [7] (see Fig. 1, left side for a typical example). However, a Fowler flap translates downstream before rotating, thereby increasing the chord and camber of the airfoil. Furthermore, high-speed fluid moves through

the gap between the main element and flap, helping to keep the flow attached. The flap also operates as a second element within the circulation of the main element, which is also advantageous aerodynamically.

The main challenge here is to develop an AFC system that can provide the necessary lift recovery for a simple hinged flap high-lift system (Fig. 1, right side) that matches the performance of a conventional Fowler flap system, while minimizing the weight and power requirements of the AFC system. Pneumatic-powered AFC concepts, such as steady blowing through discrete convergent-divergent nozzles [6] or unsteady blowing through fluidic oscillators (often referred to as sweeping jet actuators) [8–19], have been investigated around the flap shoulder region during the course of this project.

Vatsa et al. [20] previously used numerical simulations to examine the effect of geometric size and placement of actuators on the proposed CRM-SHL-AFC configuration and assess the lift augmentation potential. Flow simulations were performed for two different actuator arrangements. The first configuration examined in Ref. [20] consisted of 3 rows of fluidic actuators (sweeping jets) on the inboard flap. Due to space limitations, only 2 rows of actuators were placed on the outboard flap. The lift curve plateaued and indicated a slight drop in lift beyond nozzle pressure ratio (NPR) of 2.0 for this configuration. In the second arrangement, 2 rows of slightly larger actuators were placed on the inboard flap, leaving the outboard flap AFC arrangement unchanged. For this configuration, the lift increased monotonically with increasing NPR, although the slope of the lift curve was reduced for NPR>2.0, as reported in Figs. (17-18) of Ref. [20]. Based on the results of Ref. [20], it was concluded that using 2 rows of slightly larger actuators was more efficient in terms of attaining lift augmentation per unit mass of air flowing through the AFC system compared to 3 rows of smaller actuators. Examination of the flow field data also suggested that the flow exiting the actuators should be more tangential to the flap surface for higher effectiveness.

A team of researchers led by Dr. John C. Lin conducted wind tunnel tests of several variants of the CRM-HL and CRM-SHL-AFC configurations in the 14- by 22-Foot Subsonic Tunnel (14×22) at the NASA Langley Research Center (LaRC). Key results from their experimental study are documented in a companion paper at this conference [21]. The current numerical study has been closely coordinated with the experimental work of Lin et al. [21], and the pretest computations documented here along with the work of Ref. [20] were helpful in assessing the efficiency of actuator configurations so that only the most promising configurations needed to be tested in the wind tunnel.

II. Configuration and Computational Setup

The geometry under consideration in this paper corresponds to the 10%-scale, semispan model of the AFC-enabled high-lift configurations that are based on the "open" NASA Common Research Model (CRM) [22, 23], and they share most of the components from the conventional CRM-HL configuration that was based on the design of Lacy and Sclafani [24]. However, the Fowler flap is replaced by a simple hinged flap with embedded AFC actuators, and this AFC-enabled configuration is known as CRM-SHL-AFC. Three different types of AFC devices examined in the wind-tunnel tests are the Double-Row Sweeping Jets (DRSWJ), the Alternatingly Pulsed Jets (APJ), and the High Efficiency Low Power (HELP) actuators. These AFC devices are housed inside 4 cartridges for the inboard flap, and 6 cartridges for the outboard flap, for a total of 10 interchangeable cartridges. All of the major components of the current AFC-enabled CRM-SHL configuration, such as, slats, main wing, fuselage, nacelle-pylon and flaps are shown in Fig. 2. The DRSWJ, APJ and HELP actuators from one of the inboard cartridges are shown on the right hand side of Fig. 2 for comparison purposes. A more detailed view of the DRSWJ actuator arrangement on the flaps is presented in Fig. 3, where the feed tubes connected to the 4 inboard and the 6 outboard chambers are shown. Similar arrangement of feed tubes and cartridge chambers is also used for the HELP and the APJ actuators. Compressed air is pumped through these feed tubes for flow control. Since the actuators are fabricated as integral parts of modular cartridges, different actuators can be easily installed on the CRM-SHL-AFC model. Simulations were not performed at this time for the APJ actuators, which are in the early stages of development.

As the name implies, the DRSWJ actuator configuration uses two rows of sweeping jet actuators, and its design benefitted from the experience gained from the numerical study of Reference [20]. In the HELP configuration, the second row of sweeping jet actuators in the DRSWJ setup are replaced with thin blowing slots. The initial HELP configuration consisted of continuous slots. However, based on preliminary simulations and structural considerations, the continuous slots were replaced with discreet slots for improved efficiency. As conjectured by Lin et al. [21], the purpose of the HELP configuration is to enable the SWJ actuators of Row 1 to "precondition the boundary layer" with a small amount of air flow such that the Row 2 actuators can achieve much better flow control authority. Compressed air is fed to the actuators placed inside the AFC cartridges

through separate feed tubes to control flow separation on the highly deflected flap (50°/55° inboard/outboard flap deflection), and to recover the lift characteristics comparable to the conventional CRM-HL configuration.

The semispan of the wing is 115.675 inches, and the mean aerodynamic chord in the stowed (cruise) configuration is 27.58 inches at a span station of 46.875 inches. The wing reference area (S) used for normalizing force coefficients is 2973.6 square inches. The computations are performed at a freestream Mach number of 0.2, and Reynolds number of 3.27 million based on mean aerodynamic chord (MAC) of the model, corresponding to the test conditions at the NASA LaRC's 14×22 tunnel. The model is installed on top of a 3.5-inch-thick peniche (standoff), and can be rotated to change the angle of attack (α) of the model relative to the incoming stream. Computations are performed for the in-tunnel mode to facilitate a direct comparison with the experimental data acquired in the solid wall tunnel. A simplified approach is used for modeling the wind tunnel for in-tunnel simulations, where the CRM model is enclosed inside the rectangular test section of the wind tunnel. Slip boundary conditions are imposed on the tunnel walls and the floor up to the peniche, and velocity and temperature are imposed on the tunnel inflow boundary. No-slip boundary conditions are applied on the peniche and all of the exposed solid surfaces of the configuration. Static pressure is specified at the wind tunnel outlet for the downstream boundary condition.

To simulate the flow in the fluidic actuators, total pressure and temperature inflow boundary conditions are imposed at the inlet faces of the feed tubes (see Fig. 3) that are connected to the AFC cartridges, and the complete flow field developing inside the chambers and actuators is computed as an integral part of the overall solution for the entire configuration. Due to the bistable nature of flow inside the fluidic actuators, unsteady oscillating jets emanate from the actuator exit nozzles. For the HELP configuration, the flow also exits through an array of discrete blowing slots that are situated downstream of the fluidic actuators. The high-momentum flow exiting the actuator nozzles (and slots) energizes and interacts with the external flow over the flap surface, which results in reduced reversed flow regions and increased lift.

III. Simulation Method

Numerical simulations presented in this paper have been performed using the PowerFLOW® code, which is a compressible flow solver based originally on the three-dimensional 19-state (D3Q19) Lattice Boltzmann Method (LBM). The PowerFLOW® code represents LBM-based CFD technology developed over the last 30 years [25–29], and has been extensively validated for a wide variety of applications ranging from academic direct numerical simulation (DNS) cases to industrial flow problems in the fields of aerodynamics [30] and aeroacoustics [31]. In contrast to methods based on the classical Navier-Stokes (N-S) equations, LBM uses a simpler and more general physics formulation at the mesoscopic level [25]. As shown in Refs. [32, 33], the LBM equations recover the macroscopic hydrodynamics of the Navier-Stokes equations through the Chapman-Enskog expansion.

The PowerFLOW® code can be used to solve the Lattice Boltzmann equation in a DNS mode [34], where all of the turbulent scales are spatially and temporally resolved. However, for most engineering problems at high Reynolds numbers, the simulations are usually conducted in conjunction with a hybrid turbulence modeling approach where the smaller scales are modeled and larger, energy-containing scales are directly resolved. For the current work, the Lattice Boltzmann Very Large Eddy Simulation (LB-VLES) approach described in Refs. [27], [28] and [35] is used. Because the flow inside the actuator nozzles is expected to choke and become supersonic for higher input pressure cases, all of the results presented here were simulated with the transonic version of the PowerFLOW® code [36–38] for consistency.

The Lattice Boltzmann equation is solved on embedded Cartesian meshes, which are generated automatically within the flow solver for the configuration under consideration. Variable Resolution (VR) regions can be defined to allow for local mesh refinement of the grid by successive factors of two in each direction [25]. To reduce the resolution requirement near solid surfaces for high Reynolds number flows, a hybrid wall function is used to model the near-wall region of the boundary layer [30, 39]. The PowerFLOW® code scales well on modern computer clusters consisting of thousands of processors, making it suitable for large scale applications.

The PowerFLOW® code uses explicit time marching to solve the governing equations in a time consistent manner. The time step used for advancing the solutions is based on stability considerations. The solution on a given VR level is updated twice as often when compared to the number of solution updates on the next coarser VR level. Thus, the solution on the finest grid is updated most frequently, whereas the solution on the coarsest grid is updated least often to advance the solution in the whole domain to the same physical time. A comparable number of voxels (cells) on coarser grid levels are therefore less expensive from a computational point of view.

IV. Results

The computations of the three-dimensional (3-D) flow field for AFC-enabled CRM-SHL configurations (DRSWJ and HELP) enclosed inside the 14×22 wind tunnel have been performed using the transonic version of the PowerFLOW® code. Whereas the DRSWJ configuration consists of two rows of fluidic actuators on the inboard and outboard flaps for flow control, the second row is replaced by a set of discrete slots in the HELP configuration. The computational setup has the flexibility to turn on or off the air supply to any of the 10 chambers or to the individual actuators, thus making it convenient to examine the effect of flow control on selected portions of the flaps. Taking advantage of this capability, computations were also performed by blocking the air supply to alternate actuators in the DRSWJ cartridges, and the resulting configuration is referred to as DRSWJ-ALT-OFF in this work.

As mentioned in an earlier section, the computations are performed on embedded Cartesian meshes, which are generated in a preprocessing step. For the current configuration, a total of 13 VR regions are used, where a finer resolution was specified for high gradient regions, such as the suction surface of slats, main wing and flaps. The variation in grid density for lifting surfaces is illustrated in Fig. 4 with a planar cut of the grid at the semispan station of y=27.75 inches, where every other line is shown for improved clarity. Based on previous experience with the PowerFLOW® code [40], the normal spacing was chosen to produce an average value of 120 for y^+ on lifting surfaces.

The finest VR was used for discretizing the internal domain in the vicinity of the actuator nozzle throats. A minimum of 8×16 voxels (cells) were used at the throat for these simulations based on the experience gained during the grid sensitivity study conducted for a single actuator [41]. The voxels in the finest VR region have an edge length of 0.00567 inches (0.144 mm). The grid resolution used on major components and the farfield was comparable to the resolution used previously by Vatsa et al. [20] for the earlier setup of the fluidic actuators on a similar CRM-SHL-AFC configuration. In the current work, additional VR regions were also created to capture the vortical regions emanating from the slat edges, fuselage/wing and nacelle/pylon junctures, and the wing tip. The resulting grid consisted of approximately 526 and 583 million voxels for the DRSWJ and HELP configurations, respectively.

Since the flow field is inherently unsteady, the computations are run long enough in time for the flow to achieve a quasisteady state, as determined by variation of the integrated forces (e.g., lift) in time for a given case. Computations are typically run for a physical time of 0.4 seconds, which corresponds to the time required for traveling a distance of approximately 40 chord lengths. Time-averaging is performed on the unsteady data after the initial transients exit the computational domain, and the time-averaged solutions are used for making quantitative comparisons. Most cases required 120-160 hours of run time on 2548 Brodwell cores on the NAS Pleiades computer.

The simulated results are presented in two main sections. The first set includes the computations performed during the actuator design phase of the project prior to the wind tunnel tests (pretest) to assess lift-augmentation achievable by different actuator configurations. These simulations have been followed by post-test computations of the most efficient AFC actuators selected on the basis of pretest simulations. During the post-test phase of simulations, an attempt is made to match the cartridge chamber pressures observed in the experiment. The resulting solutions are compared with the measured data for integrated lift and sectional pressures to quantify the accuracy of the current simulation methodology. Streamline patterns based on simulated solutions are also presented to assess the ability of the AFC system to control flow separation on such high-lift configurations.

A. Pretest simulations: Lift augmentation assessment

The results presented in this section were completed prior to the start of wind tunnel testing. A parametric study was conducted where the nozzle pressure ratio (NPR) at the inlet feed tube was varied from 1.25 to 3.0 for the CRM-SHL-AFC configuration with embedded DRSWJ and HELP actuators. Examination of the flow inside the actuator nozzles indicated the presence of sonic flow for nozzle pressure ratios of 2.5 and higher. Simulations were also performed with the actuation being turned off completely (AFC-OFF), to serve as a baseline for assessing the effectiveness of AFC for lift augmentation. All of these computations were run at $\alpha = 8°$, which is the nominal condition for landing. In the absence of experimental data, an identical constant NPR was specified as a boundary condition at the entrance of all 10 feed tubes. Numerical solutions were also obtained for the CRM-HL configuration at the same test conditions for comparison purposes.

The variation of the lift coefficient with NPR for these configurations is shown in Fig. 5, where NPR was set equal to 1 for the AFC-OFF case for convenience. The lift corresponding to the CRM-HL configuration with Fowler flaps is also plotted in this figure as a dashed green line across the plot, and serves as the target for the

AFC-enabled (CRM-SHL-AFC) configuration. It is clear from Fig. 5 that AFC results in a significant increase in lift as NPR is increased. However, the slope of the lift curve starts leveling off at higher nozzle pressure ratios (NPR > 2.0) for the DRSWJ configurations. It is also noted that the lift increment for a given NPR is higher for the DRSWJ compared to the DRSWJ-ALT-OFF configuration, mainly because the DRSWJ has more actuators, and hence provides higher control authority. As seen from the results presented in Fig. 5, the highest level of lift for a given value of NPR was achieved with the HELP actuators. Although the lift curve slope of the HELP actuators shows a slight drop for NPR>2.0, a linear slope is maintained at higher values of NPR, making these actuators very effective for lift augmentation at higher NPR values.

To compare the relative efficiency of the different types of AFC actuators, the lift coefficient was plotted in Fig. 6 as a function of total mass flow ($\dot{m}$) used by the actuators. Results shown in this figure indicate that the DRSWJ type actuators achieve a higher lift increment at a given value of mass flow up to $\dot{m} = 0.6$ lbm/sec compared to the HELP actuators, whereas the DRSWJ-ALT-OFF actuators appear to be the most efficient configuration in terms of lift increment per unit of mass flow up to $\dot{m} = 0.35$ lbm/sec. Unfortunately, the lift curves for the DRSWJ-ALT-OFF and DRSWJ actuators start tapering off rapidly for $\dot{m} > 0.3$ and 0.5 lbm/sec, respectively, and these actuators fail to provide enough control authority to achieve the lift comparable to the equivalent CRM-HL configuration. On the other hand, the results for the HELP actuators indicate much higher lift augmentation for comparable pressure ratios, and these actuators not only match the lift levels of the CRM-HL configuration at NPR=2.5, but continue to generate even higher lift for NPR > 2.5. This performance comes at the cost of higher mass flow, as seen from Fig. 6, indicating higher mass flow usage by the HELP configuration for a given pressure ratio. Nonetheless, the performance of the HELP actuators does not seem to deteriorate much with increasing levels of NPR, and these are the only actuators that were found capable of achieving the lift levels comparable to the CRM-HL configuration.

B. Post-test simulations

As described by Lin et al. [21], a large set of experimental data was collected for the CRM-HL and CRM-SHl-AFC configurations in the 14×22 tunnel. These data included force data from balance measurements and surface C_p data along multiple spanwise and chordwise rows at the pressure ports displayed as small circles in Fig. 7. Although, no measurements are available at the feed tube entrance, pitot tubes were used to collect pressure data inside all 10 of the AFC chambers. Experimental data were acquired over a large range of angles of attack and pressure ratios.

Experimental data confirmed the initial findings based on pretest simulations that the CRM configuration embedded with the HELP actuators was the only viable option for achieving the lift levels of the conventional CRM-HL configuration. Therefore, post-test simulations were preformed only for the CRM-SHL configuration embedded with the HELP actuators. Detailed comparisons of the simulated results are presented with the experimental data for the the nominal landing approach conditions corresponding to an angle of attack (α) of 8°.

1. Integrated lift

Computations for the CRM-SHL-AFC configuration consisting of HELP actuators were repeated using finer grids in the leading edge regions compared to the grids used in the previous section in an effort to capture the sharp leading edge suction peaks. The variation of the time-averaged computed lift coefficient with NPR is compared with the measured data in Fig. 8. In the absence of measured data at the feed tubes, the first set of computational results (shown in blue) were obtained with a constant value of NPR imposed at the entrance of all 10 feed tubes, and are plotted as a function of NPR at the feed tubes. The predicted lift levels are found to be smaller than the measured values at a given NPR. If the results are plotted as a function of total mass flow ($\dot{m}$), as shown in Fig. 9, the predicted levels of lift are found to be higher compared to the measured levels at a given value of $\dot{m}$, which contradicts the trends seen in Fig. 8. To resolve this discrepancy, it became imperative to examine the pressure levels extracted from the computed flow field at the pitot tube locations in the AFC chambers for comparison with the measured data. The extracted chamber pressures corresponding to simulations performed with NPRs of 2.0 and 2.5 at the feed tubes are compared with the measured chamber pressures in Fig. 10. It is clear from results shown in Fig. 10, that the pressure levels in the chambers are much smaller compared to the feed tube pressures due to expansion in the chambers. Based on these results, the average chamber pressure corresponding to an NPR of 2.0 at the feed tubes appears to be closer to the measured chamber pressure levels at an NPR of 1.46. If we replot the lift as a function of average chamber pressure (Chamber NPR), the predicted lift curve (red line, Fig. 8) shifts towards the left, making the predicted

lift appear higher compared to experimental values at a given NPR, which is consistent with the trends observed in Fig. 9.

It is well known that direct comparisons with experimental data are not meaningful without the use of the appropriate boundary conditions. However, it is obvious from the chamber pressure comparisons of Fig. 10 that using constant NPR at the feed tubes in each cartridge is not the correct boundary condition since it is not going to replicate the measured chamber pressures and experimental conditions for any of the cases, especially in light of the large variation observed in the computed chamber pressures for constant input pressure at the feed tubes. In the absence of any experimental measurements at the feed tubes, an iterative process discussed below was devised for estimating the pressure levels at the feed tubes. As an illustration of the underlying process, the chamber pressures extracted from solutions based on simulations performed with a constant NPR of 2.0 were used to estimate the feed tube input pressure levels to recover the experimental values of chamber pressures for the NPR=2.0 case. As shown in Fig. 11, these computations (ITER#1) shown in green, produce much lower chamber pressures compared to the experimental data. The constant NPR at the feed tubes also results in a large variation in the chamber pressure levels, especially going from the inboard to the outboard chambers. For the next iteration, the input feed tube pressures were scaled by the difference of chamber pressures computed from previous iteration and the measured data. These results (ITER#2) shown in blue are fairly close to the measured chamber pressures. The process was repeated one more time using the chamber pressures obtained from ITER#2 to estimate the feed tube input pressures for the next iteration. As seen in Fig. 11, the chamber pressures obtained from the final iteration (ITER#3, shown in red) are in very close agreement with the measured data. The feed tube pressures used for obtaining these chamber pressures (ITER#3) are also plotted in Fig. 11 for comparison. It is interesting to note that the feed tube NPR levels required to match the measured chamber pressures were much higher (average NPR=2.73, shown in purple color) compared to the corresponding chamber pressures, and show a significant increase from the inboard to the outboard actuators.

Simulations were repeated for the HELP configuration using the procedure outlined in the preceeding paragraph to determine the appropriate input pressures at the feed tubes for recovering the measured chamber pressures corresponding to the NPR=1.25, 1.46, 2.0 and 2.41 cases. The lift coefficients resulting from computations performed in this manner are compared with the experimental data in Figs. 12 and 13 as a function of NPR and mass flow, respectively. Based on these results, it appears that the computed values of lift are somewhat higher compared to the measured values, and differ by a constant for a given value of $\dot{m}$. This becomes more evident if we plot the increment in lift from the AFC-OFF values (ΔC_L) for these cases, as shown in Fig. 14. Agreement between the computational results and measured data shown in Fig. 14 is very encouraging, given various uncertainties incurred during simulation of such a complex configuration in a wind tunnel environment. Based on the results presented here, it is clear that AFC with HELP actuators not only achieves the goal of matching the target lift of the CRM-HL configuration, but actually exceeds it for NPR>2. It should also be mentioned here that the flow meter used for providing the mass flow data is still being calibrated for consistency, and the experimental data for $\dot{m}$ will be updated at a later date, which would affect only the results shown in Figs. 13-14.

2. Sectional pressure comparisons

Time-averaged surface pressure coefficient (C_p) distributions were extracted at sectional cuts corresponding to the spanwise rows shown in Fig. 7. The experimental data were acquired at a discreet number of pressure taps placed along these rows. The computed values of C_p are compared with the measured data in Figs. 15 and 16 corresponding to inboard (y=27.75 inch) and outboard (y=63.8 inch) midflap span stations for different NPR levels, starting with the AFC-OFF case. In these figures, the results for the slat were shifted upstream by approximately 1.2 inches to avoid overlap between the slat and main wing leading edge regions.

The computational results are in good agreement with the measured data at both the inboard and outboard stations, and the effect of increasing NPR is well predicted over most of the slat, wing and flap surfaces. Whereas the lower surface of the wing remains insensitive to flow control, the suction pressure increases on the upper surface with increasing values of NPR. The most significant increase in suction pressure is observed in the vicinity of the slat and main wing leading edges, and the CFD results capture these trends quite accurately, as seen in Figs. 15 - 16. Other than slight overpredictions of slat and wing leading edge suction peaks, the computed pressure distributions agree quite well with the measured data on the slat and wing surfaces.

The computational results also indicate significant increases in the suction peaks at the flap leading edge with increasing levels of AFC input pressure. Unfortunately, there are not enough pressure taps on the model to

capture such peaks in the experiment, especially at the outboard stations. The CFD also predicts the correct trends for the pressure recovery in the vicinity of the flap trailing edge with increases in AFC input pressures, although there is a slight underprediction at some locations. The main difference between the inboard and the outboard span stations is the presence of even sharper peaks at the slat and the flap leading edges for higher NPR levels at the outboard station. The slight discontinuity in C_p for the y=63.8 inch station (Figs 16) at the wing/flap interface is due to the misalignment of spanwise rows for the main wing and the outboard flap.

It is interesting to note that the effect of AFC can be observed even at further outboard span sections, which do not contain any flaps or actuators. This is apparent in C_p distributions presented in Fig. 17 for y=94.74 inches ($\eta = 0.819$), where one can clearly see the increase in the suction peaks on the slat and wing leading edges with increasing levels of NPR, even though this station does not contain any actuators. Apparently, such an increase in suction peaks at outboard stations is caused by an increase in the overall circulation levels in the presence of AFC. The computed C_p distributions shown in Fig. 17 accurately track the experimentally observed trends, and are found to be in excellent agreement with the experimental data, except for slight underprediction of pressure recovery at the wing trailing edge.

C. Flow visualization

The results presented so far are based primarily on the surface pressure distributions, and one needs to look at the surface skin friction and off-surface flow characteristics to appreciate the effect of AFC on the resulting flow field. Previous studies [19, 20] indicated that flow behavior on the lower (compression) side of the lifting surfaces is relatively insensitive to AFC actuation levels, therefore, attention will be focused here on examination of the flow characteristics over the upper (suction) surfaces. The suction surface streamlines and skin friction contours based on time-averaged solutions are presented in Figs. 18–19 for progressively increasing levels of actuation, starting from the AFC-OFF case. It appears that the flow is attached over most of the wing surface even for the AFC-OFF case, where the wing leading edge shows the maximum skin friction levels. The most prominent effect of AFC is on the flaps, as seen in Figs. 18– 19. Whereas, massive separation is observed over the entire suction surface of the flaps in the absence of AFC (AFC-OFF), significant reduction is observed in the extent of the reversed flow region when AFC is applied. It is clear that the higher the actuation level (NPR), the smaller is the extent of flap separation, as is evident upon examination of orientation of the streamlines and the skin friction contour levels. Even for the highest actuation level (NPR=2.41), pockets of reversed flow and low skin friction levels are still present in between the chamber boundaries and at the Yehudi break between the inboard and outboard flaps. This is mainly due to the absence of actuators in those regions. Nonetheless, there is still a slight additional benefit in terms of mitigation of reversed flow extent by increasing NPR from 2.0 to 2.41, as seen from Fig. 19.

Next we examine the off-surface flow behavior for the same conditions at three spanwise planar cuts. Contour plots of time-averaged velocity magnitude and streamline patterns for the AFC-OFF case are compared with the AFC cases simulated with nominal input nozzle pressure ratios of 1.25, 2.0, and 2.41 in Figs. 20, 21 and 22 for planar cuts at two inboard (y=27.75 inch, 38.05 inch) stations, and at an outboard midspan (y=63.8 inch) station, respectively. Two of these spanwise locations correspond to the span stations for which surface C_p distributions were presented in Figs. 15 and 16.

The results for the midsection of the inboard flap (y=27.75 inch) shown in Fig. 20 indicate that the extent of the off-body reversed flow region is significantly reduced in the presence of AFC compared to the no actuation case. The size of the off-body reversed flow region decreases with increases in NPR used for AFC. Another effect of increasing NPR is an increase in velocity at the flap shoulder, which is consistent with the higher suction peaks observed in that region in Fig. 15. However, pockets of off-body reversed flow are still evident at this plane, even in the presence of the highest level (NPR=2.41) of actuation. Streamline patterns shown in the next figure (Fig. 21) also show a reduction in the extent of reversed flow for the flap at the y=38.05 inch span station when AFC is used. The flap separation is completely eliminated for NPR=2.0 and higher. The main effect of increasing NPR from 2.0 to 2.41 is to increase the velocity magnitude in the vicinity of the flap shoulder.

The streamline patterns for the outboard (y=63.8 inches) station shown in Fig. 22 also demonstrate the usefulness of AFC for controlling reversed flow at outboard stations for such high-lift configurations. A significant reduction in reversed flow in the vicinity of the flap is observed when AFC is used. Once again, the main advantage of increasing the NPR levels is the creation of higher velocity flow over the flap shoulder at this station, similar to what was observed for the inboard station (y=27.75 inches) in Fig. 20.

A better perspective of the overall global flow field emerges by examination of the 3-D streamlines to supplement the surface and planar flow patterns that were presented in Figs. 18–22. Such images are especially

helpful in visualizing the vortices generated by the juncture regions. Simulated 3-D flow patterns are compared in Figs. 23 (a)–(d) for several actuation levels, starting from the AFC-OFF case. Identical seeding was used in the trailing region to generate the streamlines shown in these figures. The streamline patterns shown in Fig. 23 (a) indicate massively separated flow on both the inboard, and the outboard flaps in the absence of actuation. These streamlines also indicate the presence of vortices generated by the wing/fuselage and nacelle/pylon junctures that travel in the spanwise direction toward the wing tip. A reduction in the reversed flow region, and weakening of these vortices on the inboard flap are observed for NPR=1.25 (Fig. 23 (b)). Increasing the NPR levels results in further weakening of vortices and reduction in the extent of reversed flow on the outboard flap. When the pressure ratio is increased to NPR= 2.0, the spanwise vortices from the wing root disappear completely, and flow on the inboard flap surface becomes attached. The outboard flap also appears to be mostly attached except in the vicinity of the Yehudi break, as seen in Fig. 23 (c). Small pockets of off-body separation similar to what was observed in Fig. 22 are still visible even for higher values of NPR, i.e., for NPR=2.0 and higher. It appears from Fig. 23 (d) that the effect of increasing the NPR levels from 2.0 to 2.41 on the streamline patterns and the extent of reversed flow regions is very minimal. Along with the results presented earlier in Figs. 18–22, the 3-D streamline patterns of Figs. 23 (a)-(d) are very helpful in understanding the overall flow characteristics associated with high-lift configurations, and the effectiveness of AFC for reducing the extent of reversed flow regions for such problems.

V. Concluding Remarks

Computational results based on numerical simulations performed using a fully compressible Lattice Boltzmann formulation in the PowerFLOW® CFD code are presented for an AFC-enabled simplified high-lift CRM configuration (CRM-SHL-AFC) in which the flap shoulder is embedded with fluidic actuators and discrete blowing jets for active flow control. Simulations have been performed for two different sets of actuator arrangements (DRSWJ and HELP) to assess their relative performance for lift enhancement and separation control. The entire flow field, including the flow inside the actuators, is simulated in the current approach.

Results are presented to examine the effect of varying the input pressures to the actuators on surface pressure distributions and integrated forces. The first set of results presented are based on pretest computations performed before fabrication of the test model in order to select an actuator arrangement suitable for achieving lift coefficients comparable to the conventional high-lift configuration. Based on these computational results, it was determined that the configuration embedded with the HELP actuators was better suited to achieve this objective.

The CFD code requires flow conditions at the feed tube entrance for setting the boundary conditions. Since such information is not available from experimental data, an iterative procedure was devised to replicate the experimental conditions. Computed results for the time-averaged integrated lift and sectional C_p distributions for the CRM-SHL-AFC configuration consisting of HELP actuators were compared with the experimental data from tests conducted in the NASA LaRC 14- by 22-Foot Subsonic Tunnel (14×22). Although the computational results slightly overpredicted the integrated lift, the computed lift increment relative to the nonactuated case compared well with the experimental data. In addition, the overall agreement of the computed results for the sectional distribution of pressure coefficients is considered quite good.

The results presented here clearly demonstrate the usefulness of CFD to compare the performance of different types of actuator arrangements, and thus help to design more efficient AFC configurations prior to conducting wind tunnel tests. The flow visualization available from the computational results is also helpful in understanding the effect of AFC on the surface and off-body flow separation characteristics for complex configurations.

Future studies should focus on grid refinement studies to reduce the uncertainty in the computational results. Parametric studies encompassing a broader angle of attack range should also be undertaken to assess the applicability of the current CFD methodology for predicting stall characteristics of the AFC-enabled high-lift configurations. In addition, comparisons of unsteady flow characteristics should be made with the Kulite® data acquired during the wind tunnel tests.

Acknowledgments

References

[1] Van Dam, C., "The Aerodynamic Design of Multi-Element High-Lift Systems for Transport Airplanes," *Progress in Aerospace Sciences*, Vol. 38, 2002, pp. 101–144.

[2] Greenblatt, D., and Wygnanski, I., "The Control of Flow Separation by Periodic Excitation," *Progress in Aerospace Sciences*, Vol. 36, 2000, pp. 487–545.

[3] Cattafesta III, L., and Sheplak, M., "Actuators for Active Flow Control," *Annual Review of Fluid Mechanics*, Vol. 43, 2010, pp. 247–272.

[4] McClean, J., Crouch, J., Stoner, R., Sakrai, G., Feifel, W., and Rush, H., "Study of the Application of Separation Control by Unsteady Excitation to Civil Transport Aircraft," NASA CR-1999-209338, 1999.

[5] Hartwich, P., Camacho, P., El-Gohary, K., Gonzales, A., Lawson, E., and Shmilovich, A., "System-Level Trade Studies for Transonic Transports with Active Flow Control (AFC) Enhanced High-Lift Systems," AIAA Paper 2017-0321, January 2017.

[6] Hartwich, P., Shmilovich, A., Lacy, D., Dickey, E., Sclafani, A., Sundaram, P., and Yadlin, Y., "Refined AFC-Enabled High-Lift System Integration Study," NASA CR-2016-219170, 2016.

[7] Loftin, L., "Quest for Performance - The Evolution of Modern Aircraft," NASA SP-468, https://www.hq.nasa.gov/pao/History/SP-468/ch10-5.htm, 1985.

[8] DeSalvo, M., Whalen, E., and Glezer, A., "Enhancement of a High-Lift Airfoil using Low-Power Fluidic Actuators," AIAA Paper 2010-0863, June 2010.

[9] DeSalvo, M., Whalen, E., and Glezer, A., "High-Lift Enhancement using ActiveFlow Control," AIAA Paper 2011-3355, June 2011.

[10] Woszidlo, R., and Wygnanski, I., "Parameters Governing Separation Control with Sweeping Jet Actuators," AIAA Paper 2011-3172, June 2011.

[11] Vatsa, V., Koklu, M., Wygnanski, I., and Fares, E., "Numerical Simulation of Fluidic Actuators for Flow Control Applications," AIAA Paper 2012-3239, June 2011.

[12] Seele, R., Graff, E., Gharib, M., Taubert, L., Lin, J., and Wygnanski, I., "Improving Rudder Effectiveness with Sweeping Jet Actuators," AIAA Paper 2012-3244, June 2012.

[13] Seele, R., Graff, E., Lin, J., and Wygnanski, I., "Performance Enhancement of a Vertical Tail Model with Sweeping Jet Actuators," AIAA Paper 2013-0411, January 2013.

[14] Graff, E., Seele, R., Lin, J., and Wygnanski, I., "Sweeping Jet Actuators - A New Design Tool for High Lift Generation," NATO Workshop on Innovative Control Effectors for Military Vehicles (AVT-215), 2013. Stockholm, Sweden, May 20–22.

[15] Gregory, J., and Tomac, M., "A Review of Fluidic Oscillator Development and Application for Control," AIAA Paper 2013-2474, June 2013.

[16] Melton, L., and Koklu, M., "Active Flow Control Using Sweeping Jet Actuators on a Semi-Span Wing Model," AIAA Paper 2016-1872, January 2016.

[17] Melton, L., Koklu, M., Andino, Y., M., Lin, J., and Edelman, L., "Sweeping Jet Optimization Studies," AIAA Paper 2016-4233, June 2016.

[18] Jones, G., Milholen, W., Chan, D., and Goodliff, S., "A Sweeping Jet Application on a High Reynolds Number Semi-Span Supercritical Wing Configuration," AIAA Paper 2017-3044, June 2017.

[19] Vatsa, V., Casalino, D., Lin, J., and Appelbaum, J., "Numerical Simulation of a High-Lift Configuration with Embedded Fluidic Actuators," AIAA Paper 2014-2142, June 2014.

[20] Vatsa, V., Duda, B., Lin, J., Melton, L., and O'Connell, M., "Numerical Simulation of a Simplified High-Lift CRM Configuration Embedded with Fluidic Actuators," AIAA Paper 2018-3063, June 2018.

[21] Lin, J., Melton, L., Hannon, J., Andino, K. M., M.Y., Paschal, K., and Vatsa, V., "Wind Tunnel Testing of Active Flow Control on High Lift Common Research Model," Paper to be presented at the 2019 AIAA Aviation Conference, June 2019.

[22] Vassberg, J., DeHaan, M., Rivers, S., and Wahls, R., "Development of a Common Research Model for Applied CFD Validation Studies," AIAA Paper 2008-6919, August 2008.

[23] NASA Common Research Model, URL: http://commonresearchmodel.larc.nasa.gov, last accessed, July 2019.

[24] Lacy, D., and Sclafani, A., "Development of the Common Research Model (HL-CRM): A Representative High Lift Configuration for Transonic Transports," AIAA Paper 2016-0308, January 2016.

[25] Chen, H., "Volumetric Formulation of the Lattice Boltzmann Method for Fluid Dynamics: Basic Concept," *Physical Review A*, Vol. 58, 1998, pp. 3955–3963.

[26] Chen, H., Teixeira, C., and Molvig, K., "Realization of Fluid Boundary Conditions via Discrete Boltzmann Dynamics," *Intl. J. Mod. Phys. C*, Vol. 9, No. 8, 1998, pp. 1281–1292.

[27] Yakhot, V., and Orszag, S., "Renormalization Group Analysis of Turbulence. I. Basic Theory," *J. Sci. Comput.*, Vol. 1, No. 2, 1986, pp. 3–51.

[28] Chen, H., Kandasamy, S., Orszag, S., Shock, R., Succi, S., and Yakhot, V., "Extended Boltzmann Kinetic Equation for Turbulent Flows," *Science*, Vol. 301, No. 5633, 2003, pp. 633–636.

[29] Chen, S., and Doolen, G., "Lattice Boltzmann Method for Fluid Flows," *Ann. Rev. Fluid Mech.*, Vol. 30, 1998, pp. 329–364.

[30] Fares, E., and Nölting, S., "Unsteady Flow Simulation of a High-Lift Configuration using a Lattice Boltzmann Approach," AIAA Paper 2011-869, January 2011.

[31] Khorrami, M., Fares, E., and Casalino, D., "Towards Full-Aircraft Airframe Noise Prediction: Lattice-Boltzmann Simulations," AIAA Paper 2014-2481, June 2014.

[32] Chen, H., Chen, S., and Matthaeus, W., "Recovery of the Navier-Stokes Equations Using a Lattice-gas Boltzmann Method," *Physical Review A*, Vol. 45, 1992, pp. 5339–5342.

[33] Qiana, Y. H., D'Humiéres, D., and Lallemand, P., "Lattice BGK Models for Navier-Stokes Equations," *Europhysics Letters*, Vol. 17, 1992, pp. 479–484.

[34] Li, Y., Shock, R., and Chen, H., "Numerical Study of Flow Past an Impulsively Started Cylinder by Lattice Botzmann Method," *J. Fluid Mech.*, Vol. 519, 2004, pp. 273–300.

[35] Chen, H., Orszag, S., Staroselsky, I., and Succi, S., "Expanded Analogy between Boltzmann Kinetic Theory of Fluid and Turbulence," *J. Fluid Mech.*, Vol. 519, 2004, pp. 301–314.

[36] Shan, X., Yuvan, X.-F., and Chen, H., "Kinetic Theory Representation of Hydrodynamics: a Way Beyond the Navier-Stokes Equation," *Physics. Rev. Lett.*, Vol. 80, 1998, pp. 65–88.

[37] Zhuo, C., Zhong, C., Li, K., Xiong, S., Chen, X., and Cao, J., "Application of Lattice Boltzmann Method to Simulation of Compressible Turbulent Flow," *Commun. Comput. Physics*, Vol. 8, 2010, pp. 1208–1223.

[38] Fares, E., Wessels, M., Li, Y., Gopalakrishnan, P., Zhang, R., Sun, C., Gopalaswamy, N., Roberts, P., Hoch, J., and Chen, H., "Validation of a Lattice Boltzmann Approach for Transonic and Supersonic Simulations," AIAA Paper 2014-0952, January 2014.

[39] Fares, E., "Unsteady Flow Simulation of the Ahmed Reference Body using a Lattice Boltzmann Approach," *Comput. Fluids*, Vol. 35, No. 8-9, 2006, pp. 940–950.

[40] Fares, E., Duda, B., Ribeiro, A., and König, B., "Scale-resolving simulations using lattice Boltzmann-based approach," *CEAS Aeronautical Journal*, 2018. Http://dx.doi.org/10.1007/s13272-018-0317-0.

[41] Duda, B., Fares, E., Wessels, M., and Vatsa, V., "Unsteady Flow Simulation of a Sweepig Jet Actuator Using a Lattice-Boltzmann Method," AIAA Paper 2016-1818, January 2016.
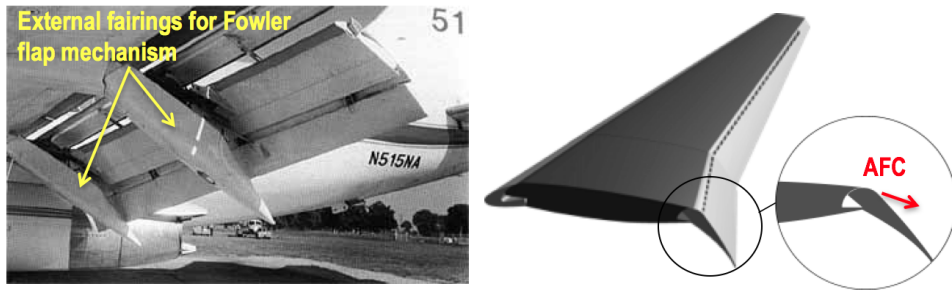
Fig. 1   Schematic of Fowler and simple hinged flaps
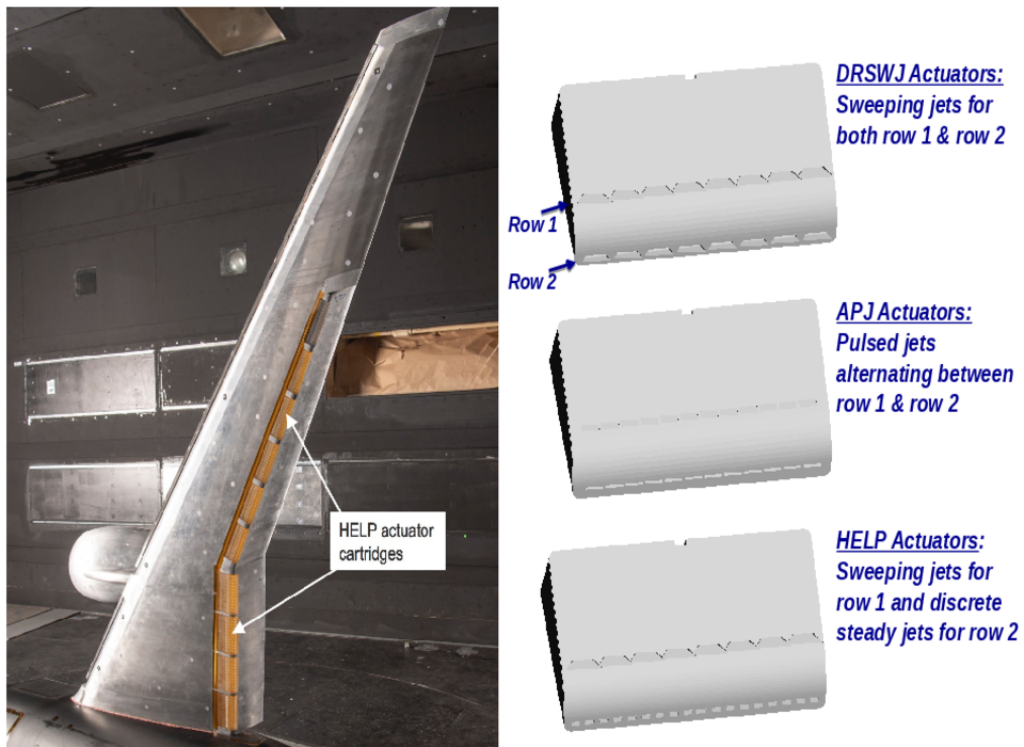
Fig. 2   Simplified high-lift CRM configuration and AFC actuators.
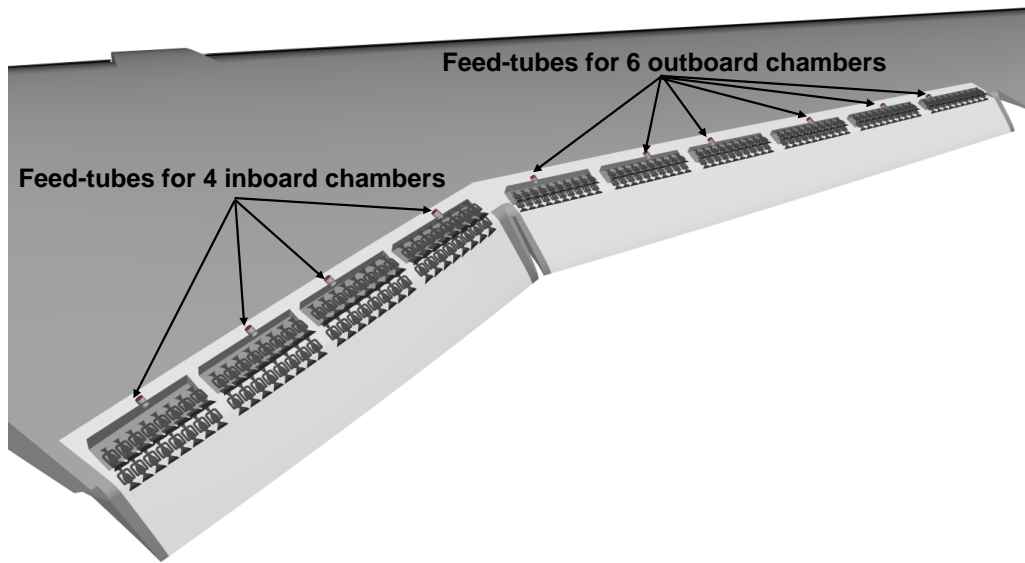
Fig. 3   Detailed view of DRSWJ actuators.
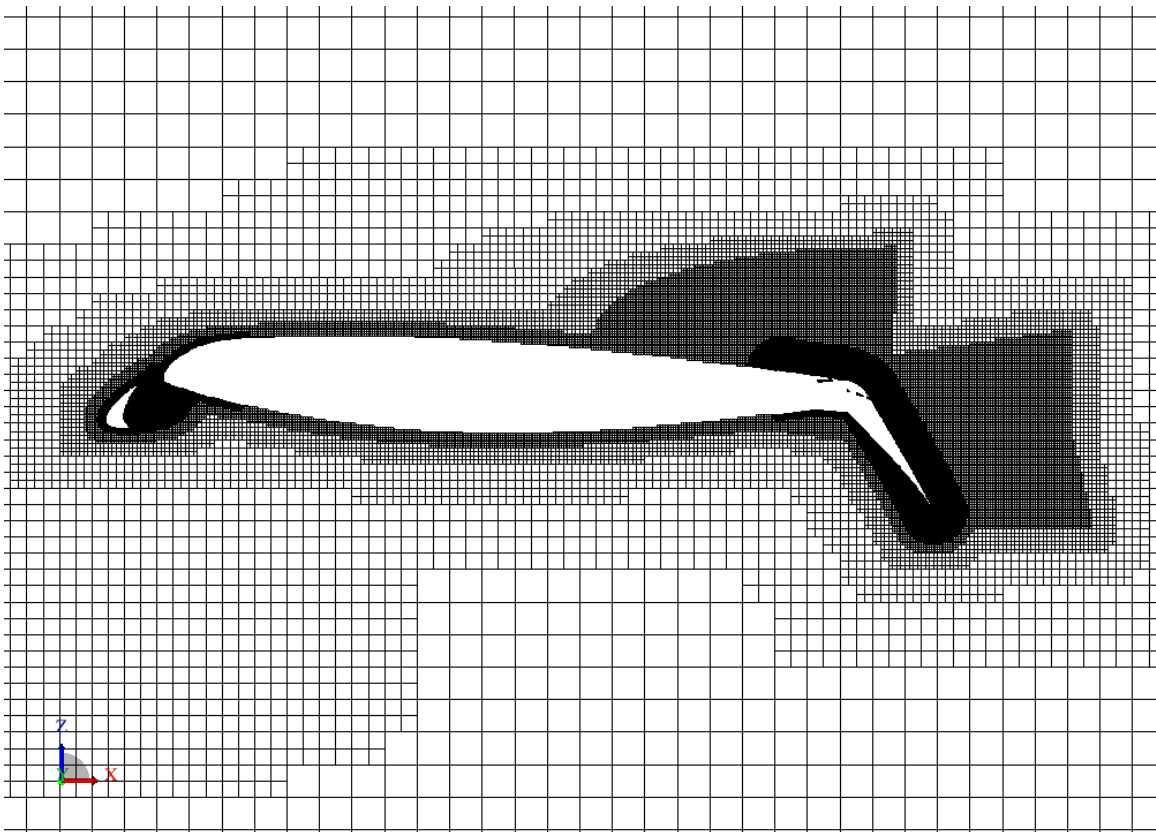
Fig. 4   Grid density variation at a planar section, y=27.75 inches.
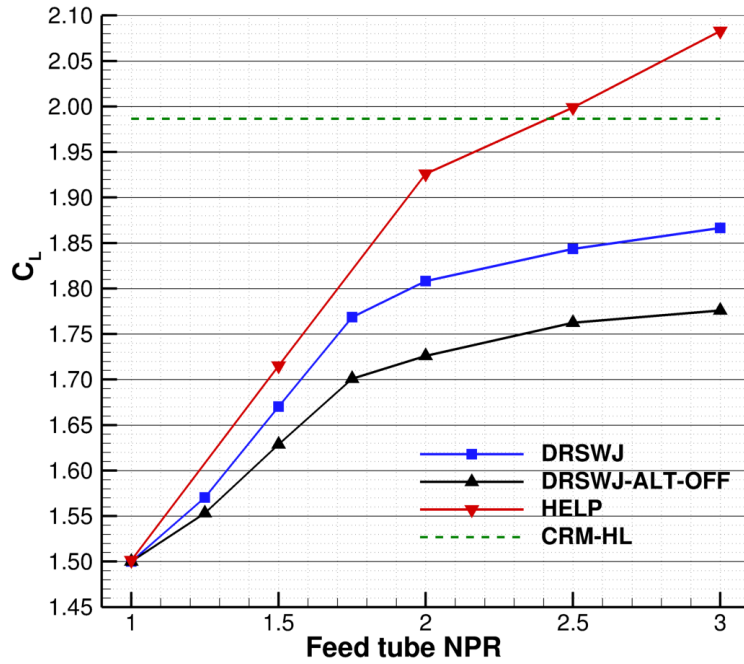
Fig. 5   Effect of feed tube pressure variation on lift coefficient for DRSWJ and HELP actuators, $Mach = 0.2, Re = 3.27 \times 10^6, \alpha = 8°$**.**
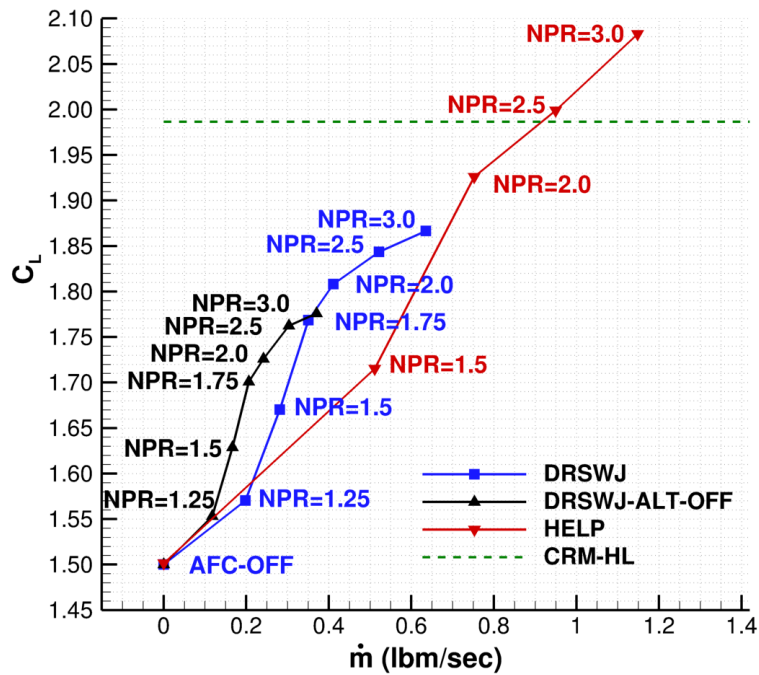
Fig. 6   Effect of input mass flow variation on lift coefficient for DRSWJ and HELP actuators, $Mach = 0.2, Re = 3.27 \times 10^6, \alpha = 8°$**.**
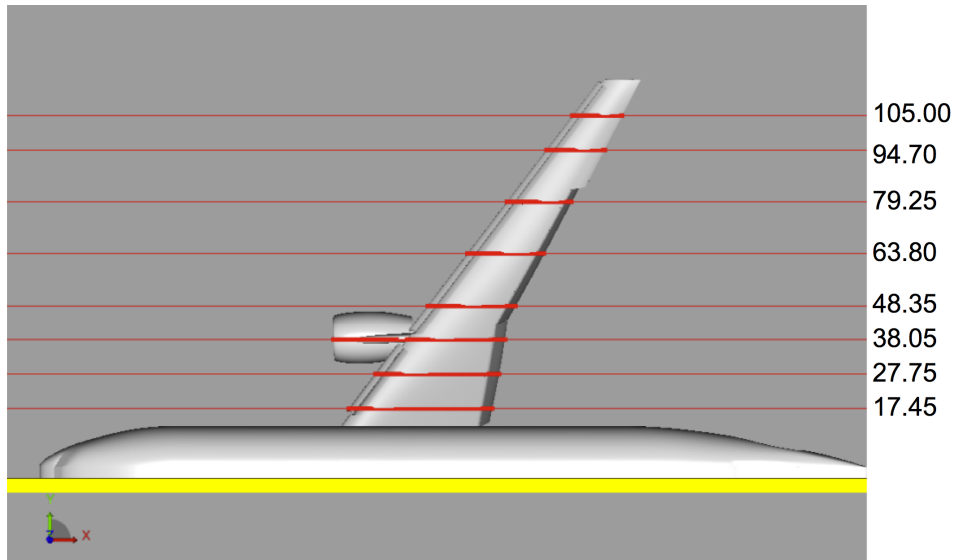
(a) Spanwise cuts
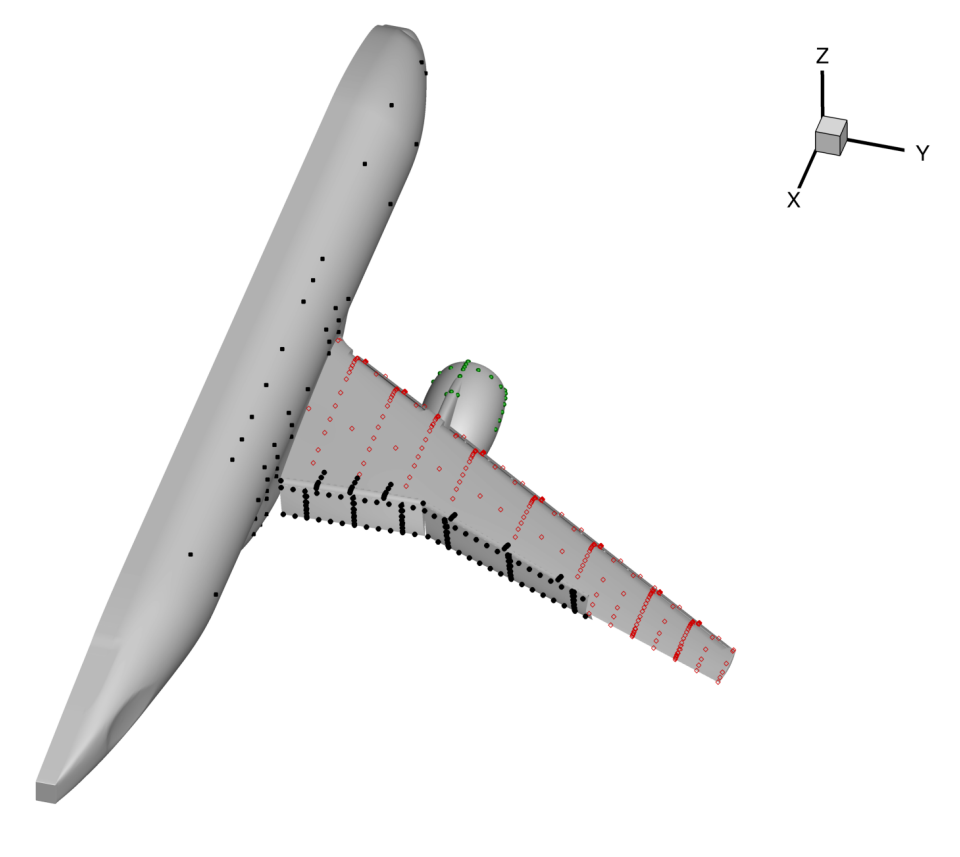
(b) Pressure ports

Fig. 7   Schematic of spanwise cuts and static pressure port locations.
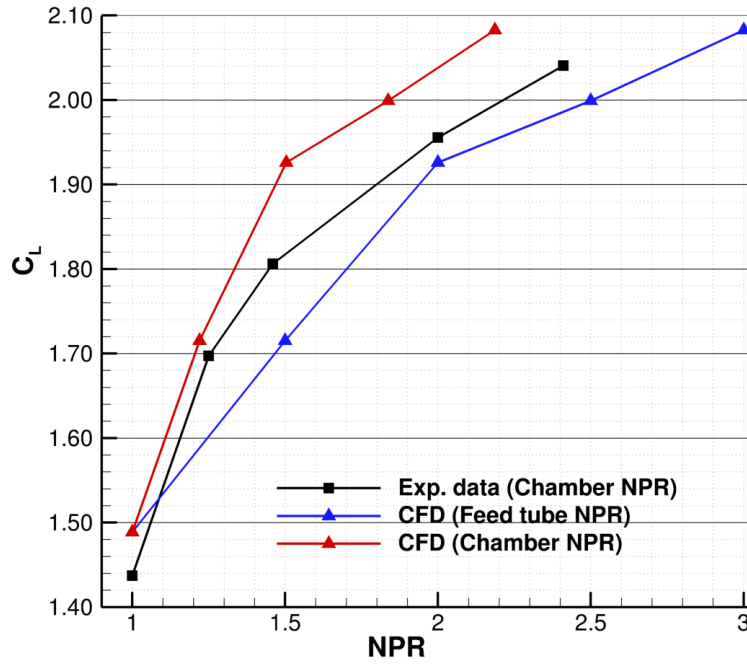
Fig. 8 Comparison of lift coefficient variation with input pressures, $Mach = 0.2, Re = 3.27 \times 10^6, \alpha = 8°$.
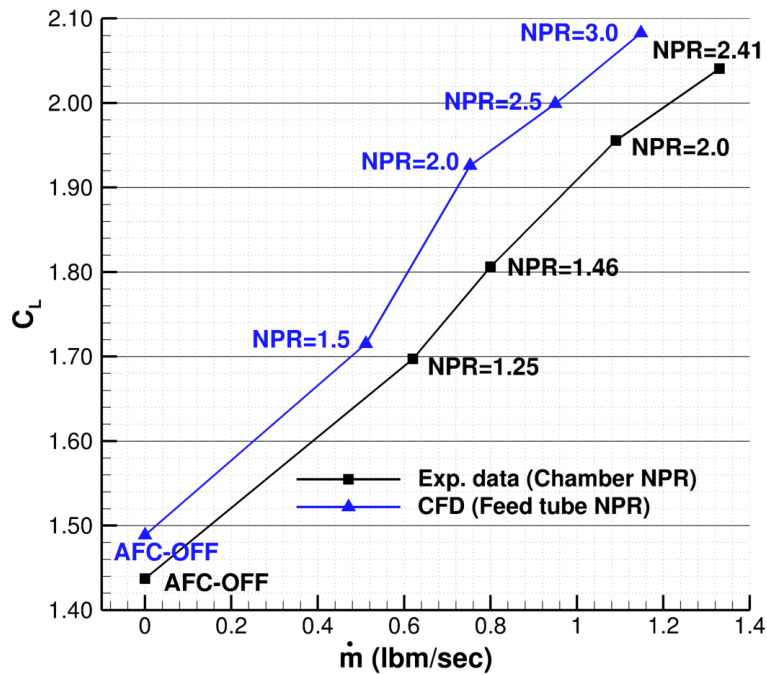
Fig. 9 Comparison of lift coefficient variation with input mass flow, $Mach = 0.2, Re = 3.27 \times 10^6, \alpha = 8°$.
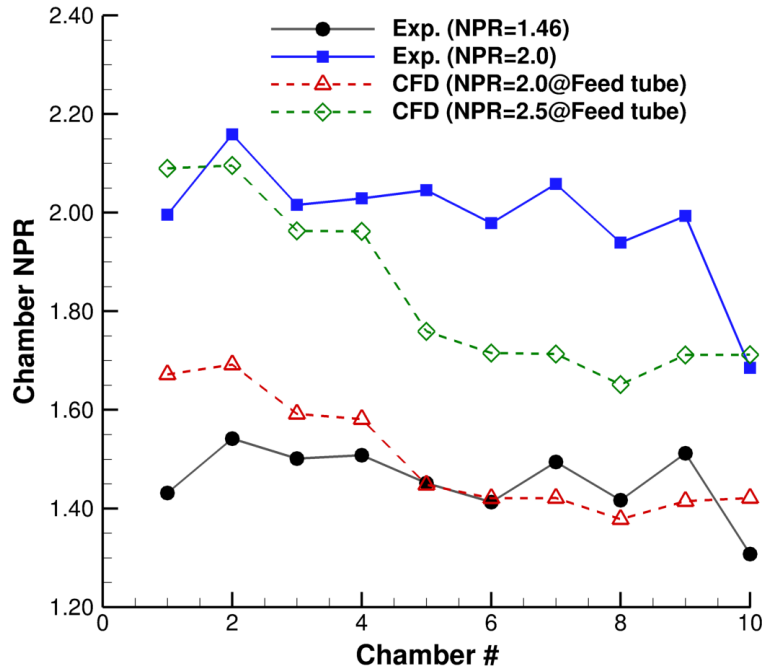
Fig. 10 **Variation of computed and measured chamber pressures for constant NPR at feed tubes,** $Mach = 0.2, Re = 3.27 \times 10^6, \alpha = 8°$.
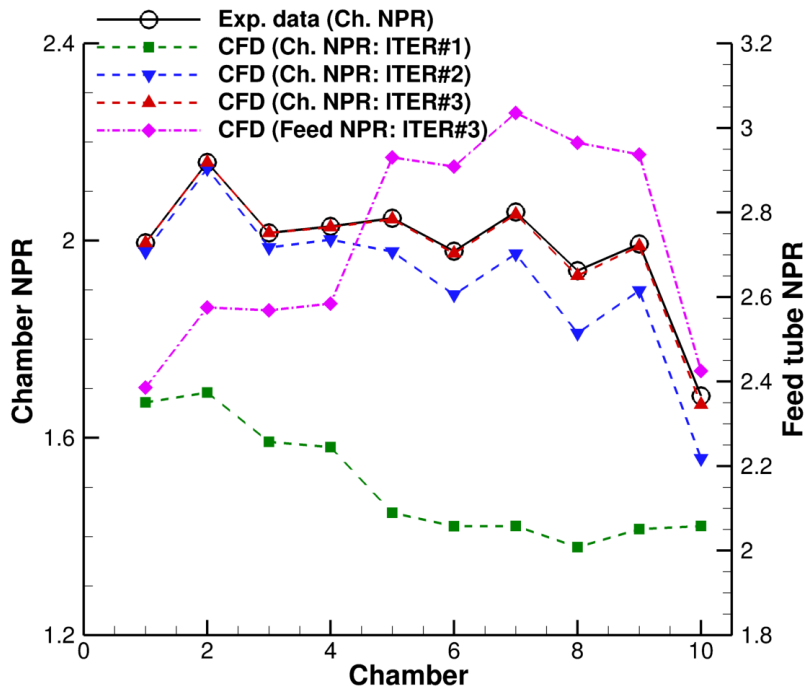
Fig. 11 **Iterative process to estimate feed tube pressures for NPR=2.0,** $Mach = 0.2, Re = 3.27 \times 10^6, \alpha = 8°$.

17
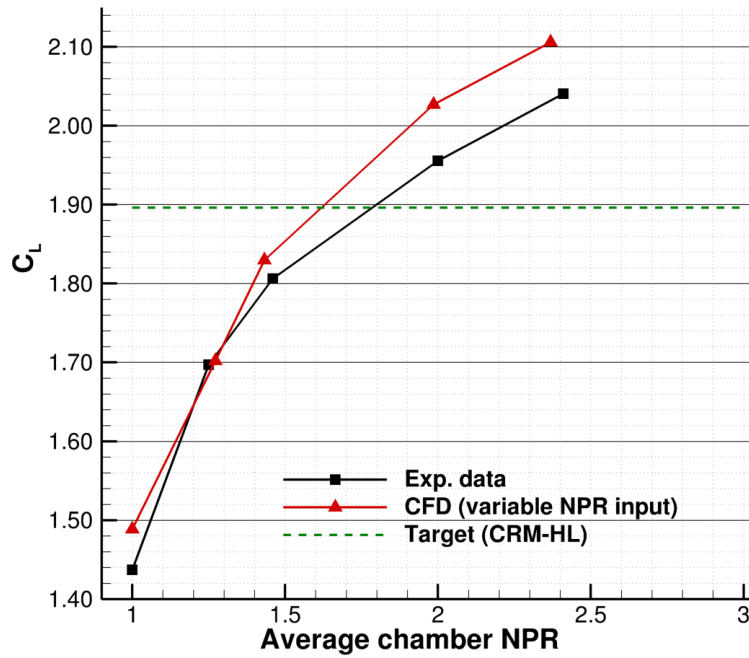
Fig. 12 **Lift coefficient variation with NPR for variable input pressures,**
$Mach = 0.2, Re = 3.27 \times 10^6, \alpha = 8°.$
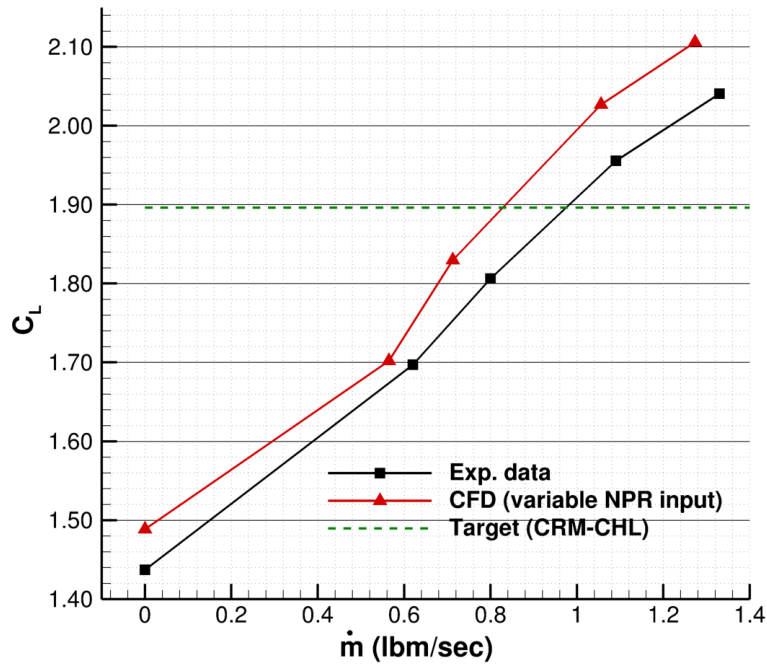
Fig. 13 **Lift coefficient variation with input mass flow for variable input pressure,**
$Mach = 0.2, Re = 3.27 \times 10^6, \alpha = 8°.$
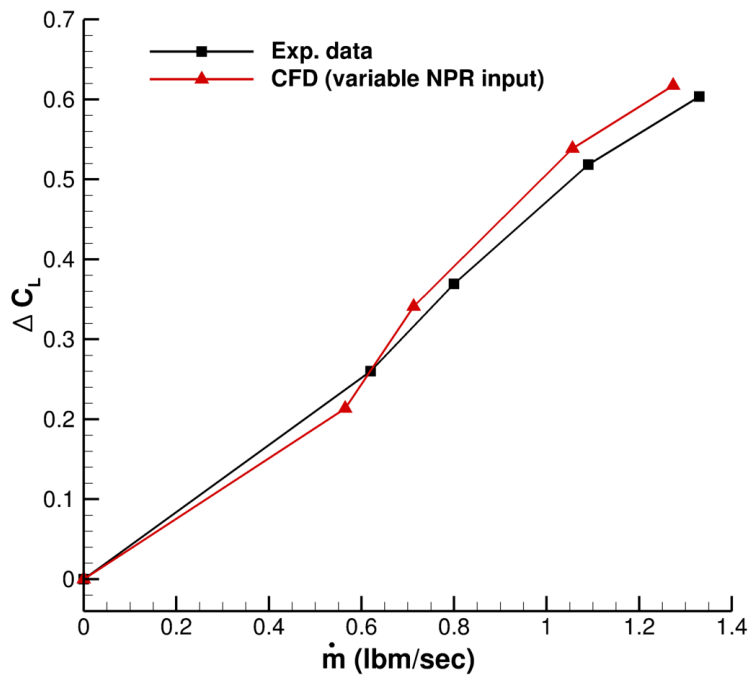
Fig. 14 Comparison of incremental lift coefficient variation with input mass flow, $Mach = 0.2, Re = 3.27 \times 10^6, \alpha = 8°.$
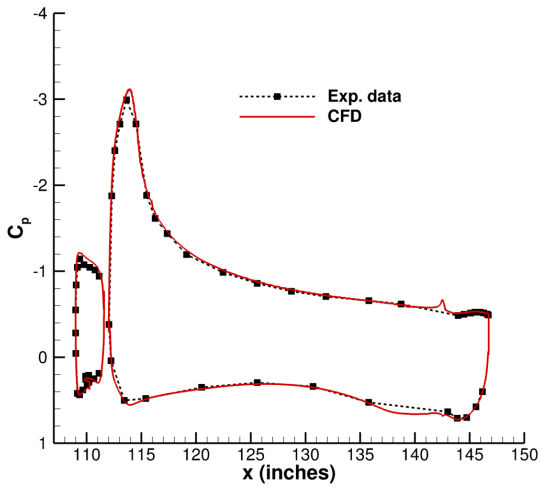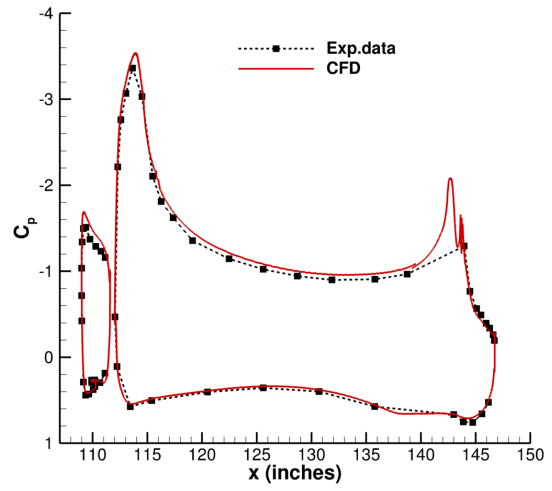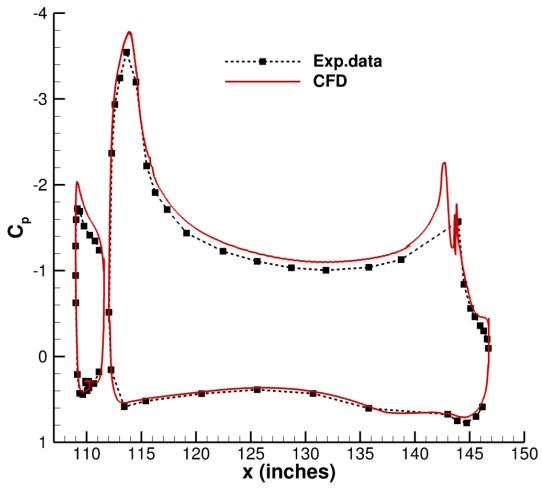
(a) AFC-OFF
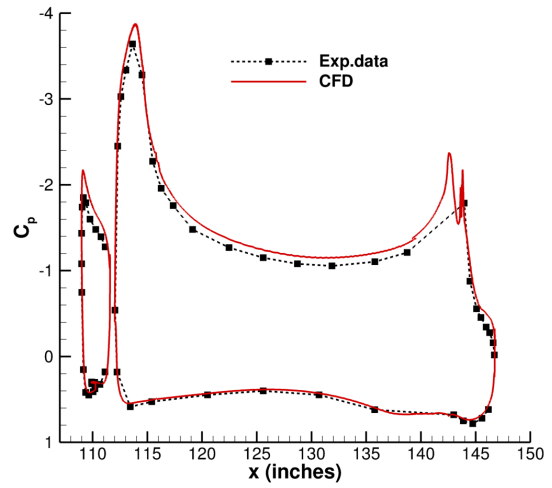
(b) NPR=1.46

(c) NPR=2.0

(d) NPR=2.41

Fig. 15   Effect of pressure variation on sectional C_p at y=27.75 inches ($\eta = 0.240$) $Mach = 0.2, Re = 3.27 \times 10^6, \alpha = 8^\circ$.
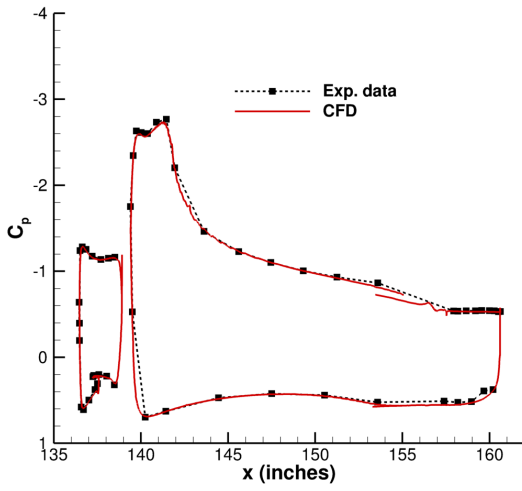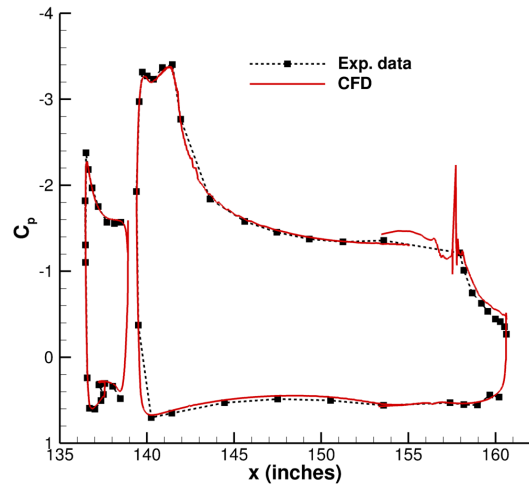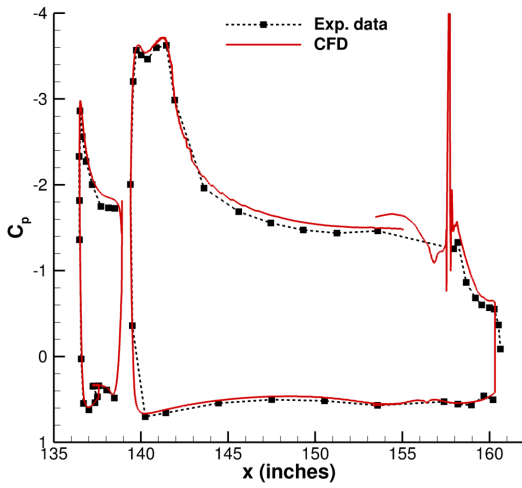
(a) AFC-OFF
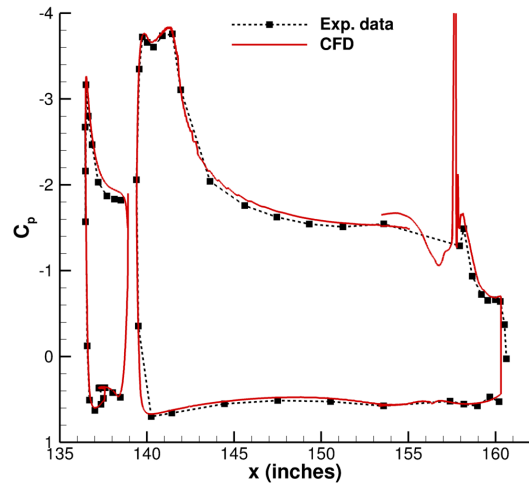
(b) NPR=1.46

(c) NPR=2.0

(d) NPR=2.41

Fig. 16 **Effect of pressure variation on sectional** C_p **at y=63.8 inches** ($\eta = 0.552$) $Mach = 0.2, Re = 3.27 \times 10^6, \alpha = 8°$.
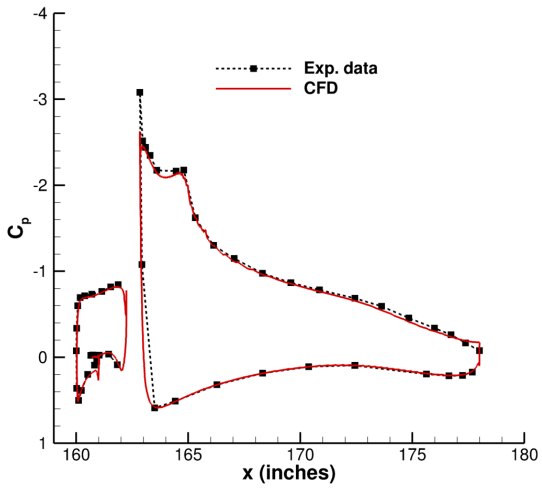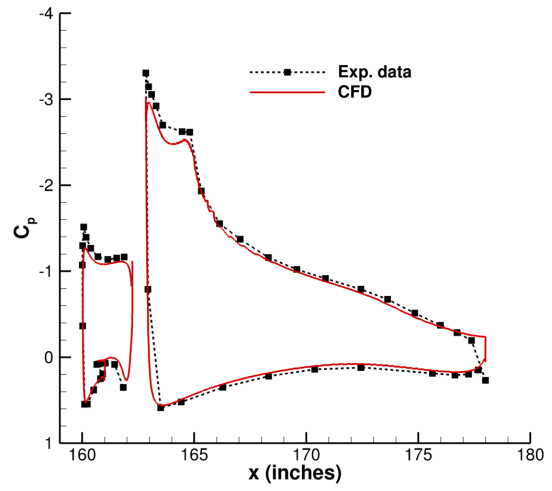
(a) AFC-OFF

(b) NPR=1.46
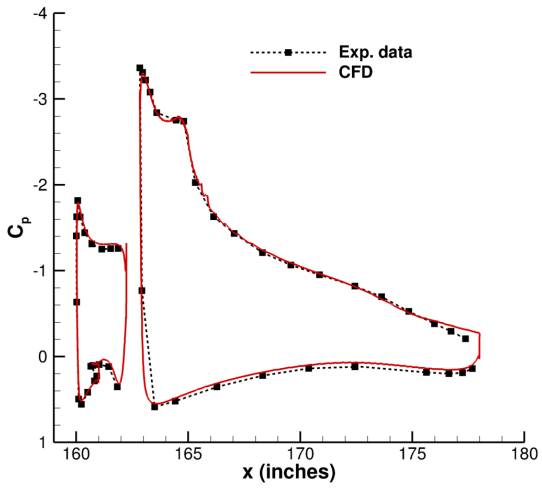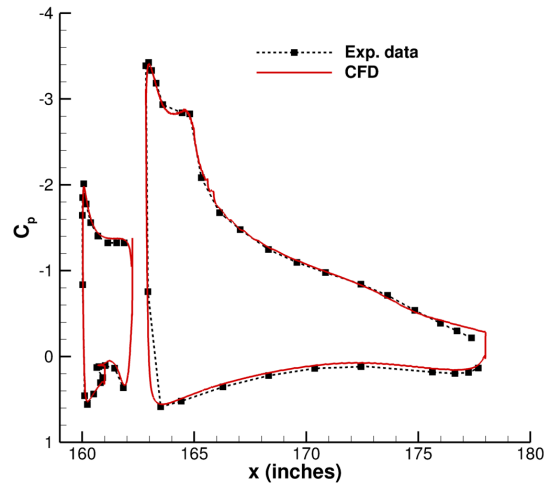
(c) NPR=2.0

(d) NPR=2.41

Fig. 17   Effect of pressure variation on sectional C_p at y=94.74 inches ($\eta = 0.819$) $Mach = 0.2, Re = 3.27 \times 10^6, \alpha = 8°$.
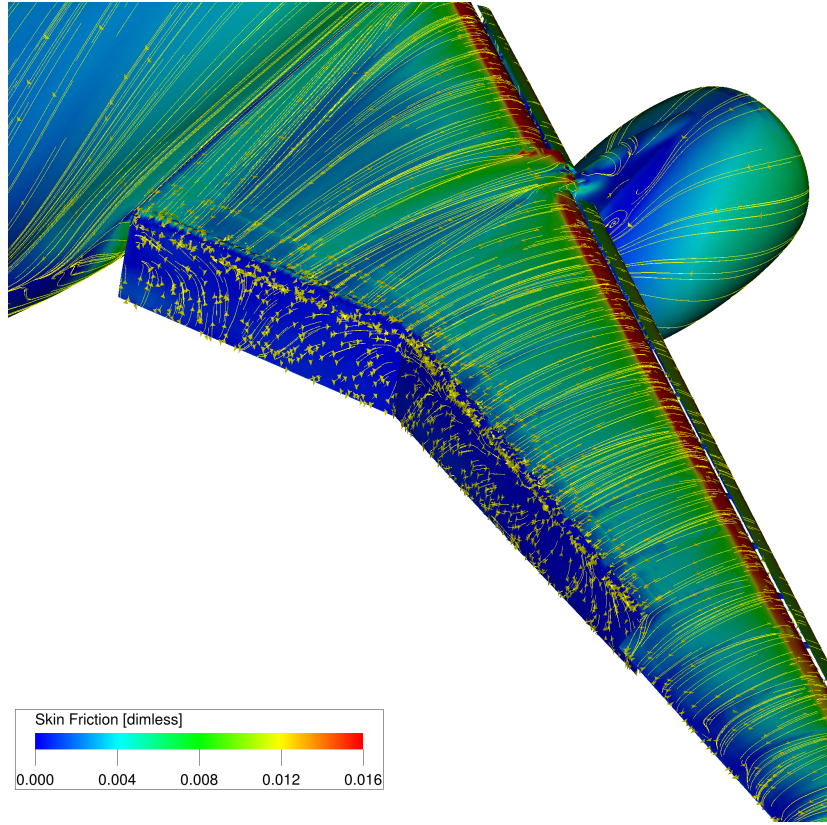
(a) AFC-OFF
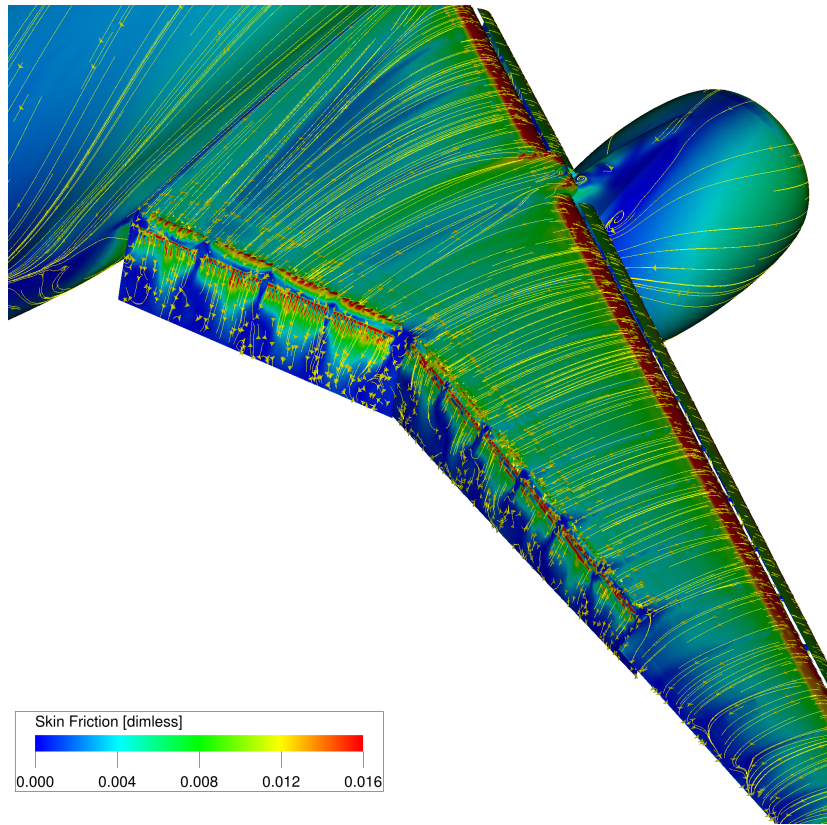
(b) AFC: NPR=1.25

Fig. 18   Effect of feed tube pressure levels on simulated surface streamline patterns, $Mach = 0.2, Re = 3.27 \times 10^6, \alpha = 8°$**, continued.**

23
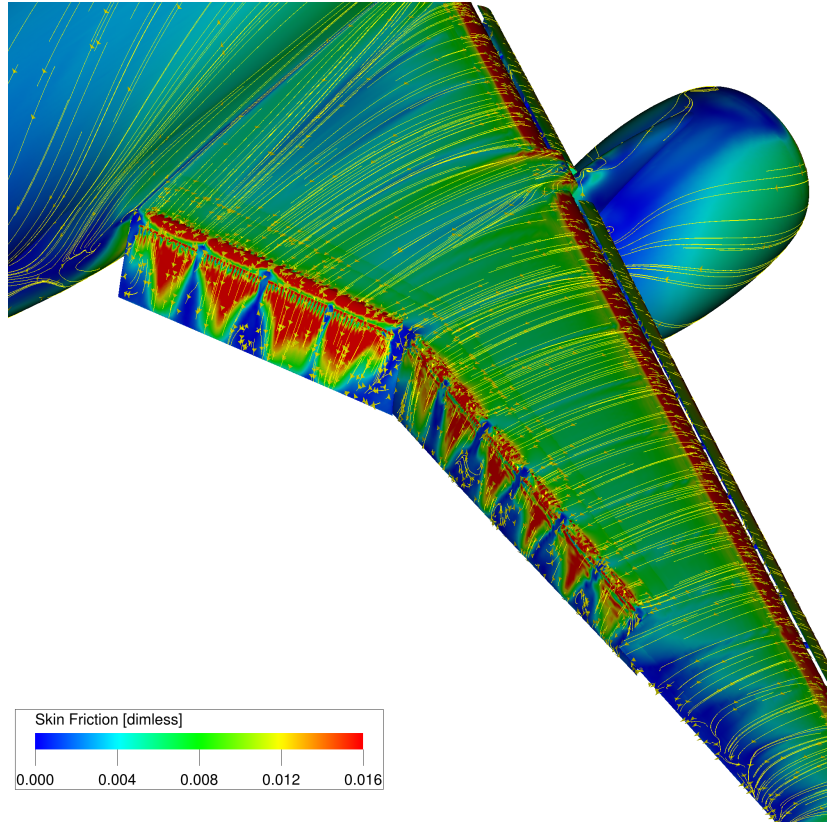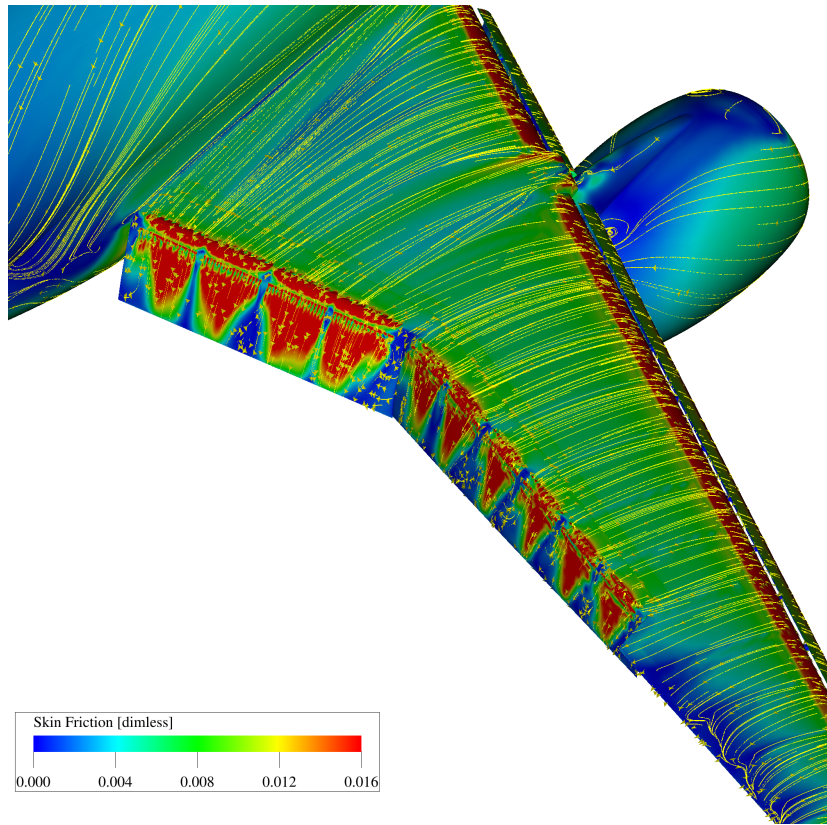
(a) AFC: NPR=2.0

(b) AFC: NPR=2.41

Fig. 19   Effect of feed tube pressure levels on simulated surface streamline patterns,
$Mach = 0.2, Re = 3.27 \times 10^6, \alpha = 8°$, **final.**

(a) AFC-OFF

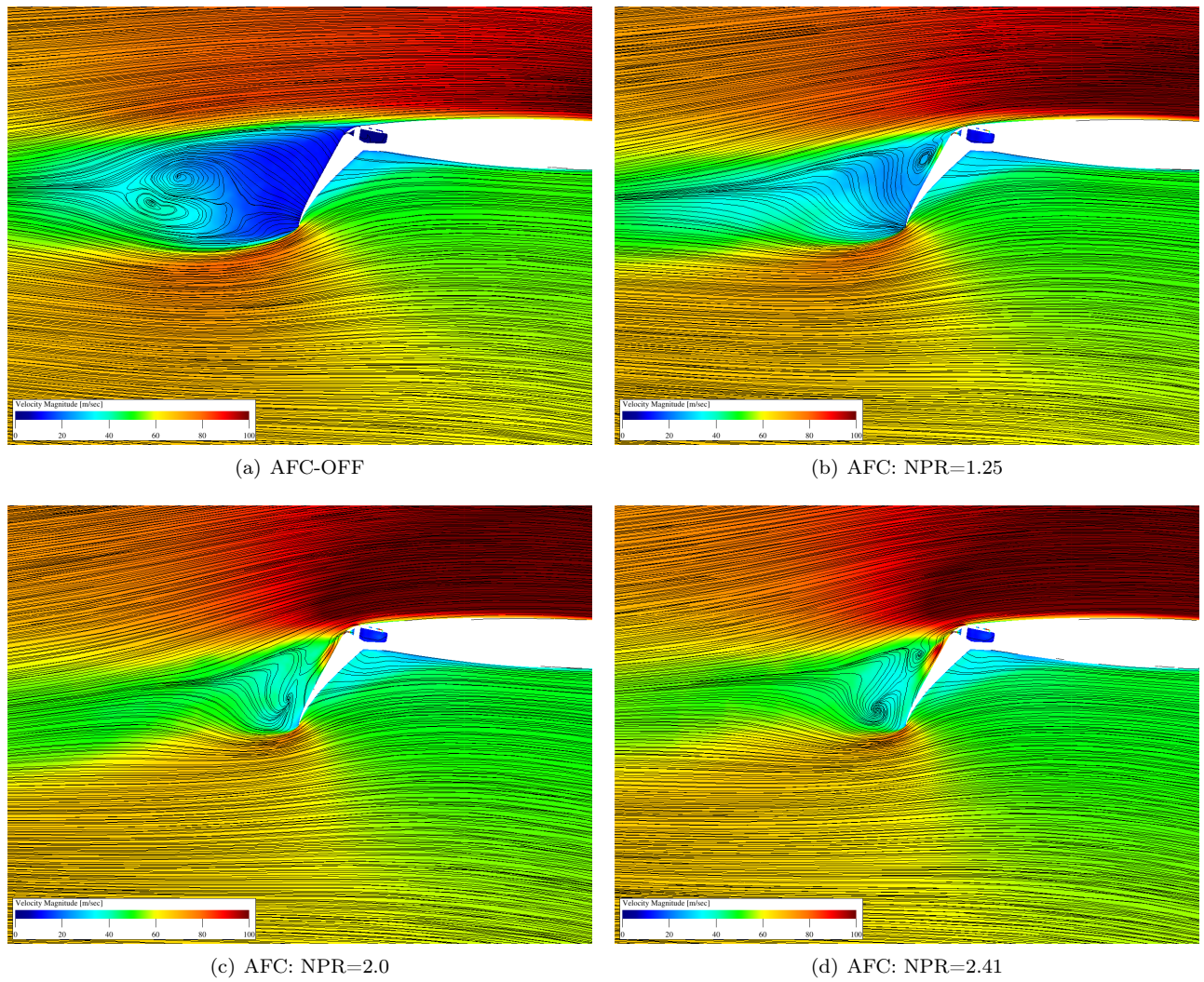(b) AFC: NPR=1.25

(c) AFC: NPR=2.0

(d) AFC: NPR=2.41
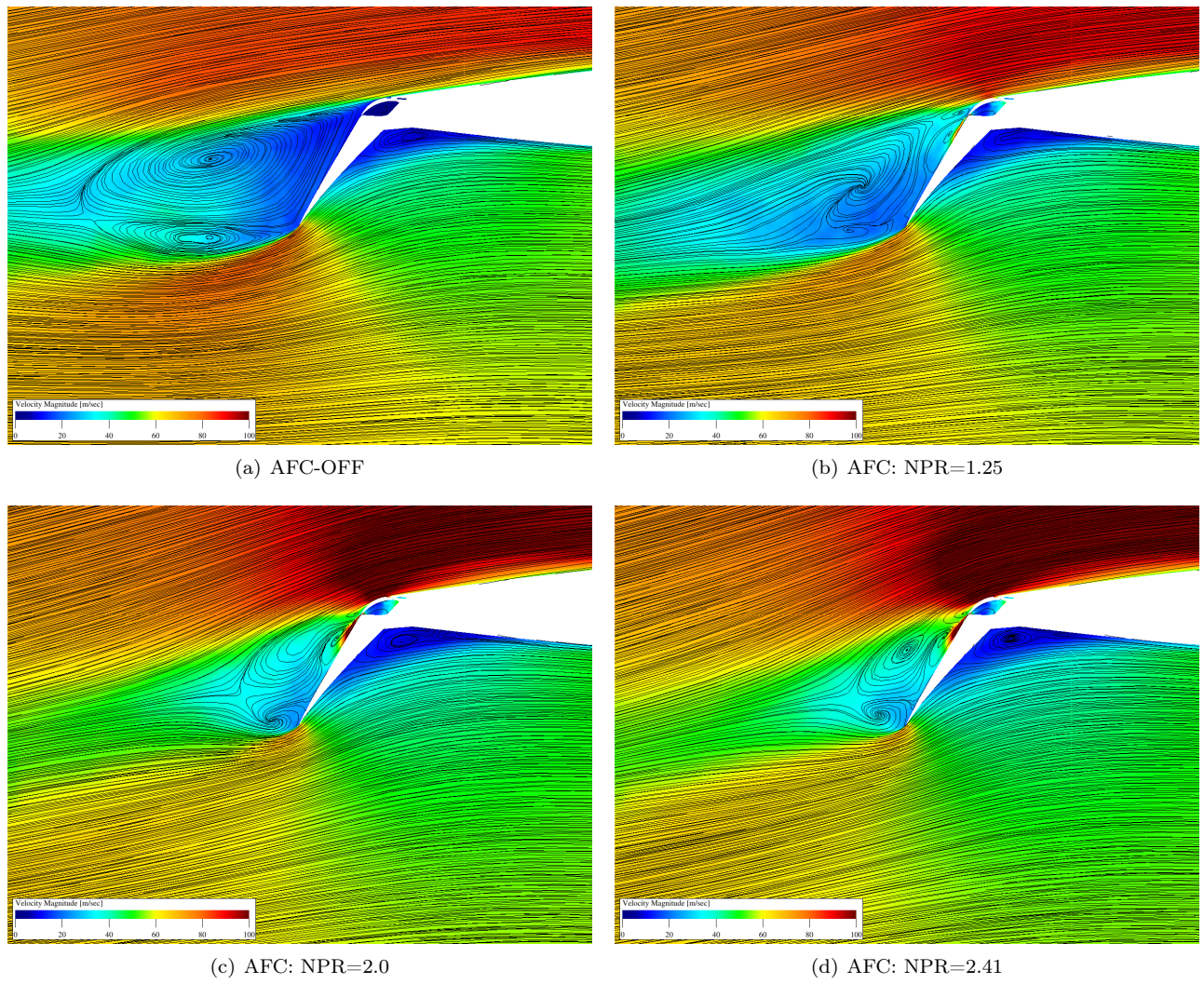
Fig. 20   Effect of input pressure levels on simulated streamline patterns, y=27.75 inches, $Mach = 0.2, Re = 3.27 \times 10^6, \alpha = 8°.$
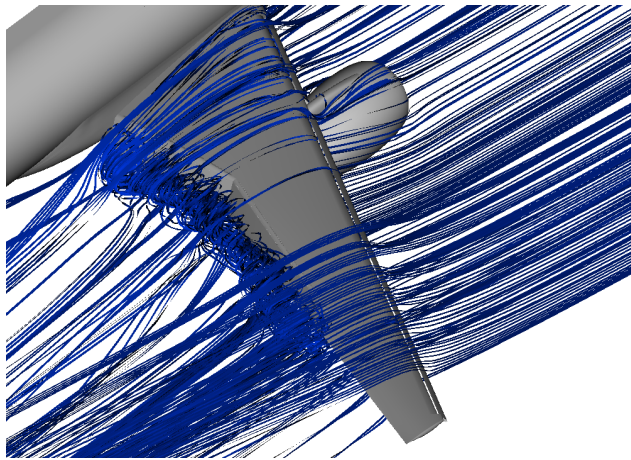
(a) AFC-OFF

(b) AFC: NPR=1.25

(c) AFC: NPR=2.0

(d) AFC: NPR=2.41
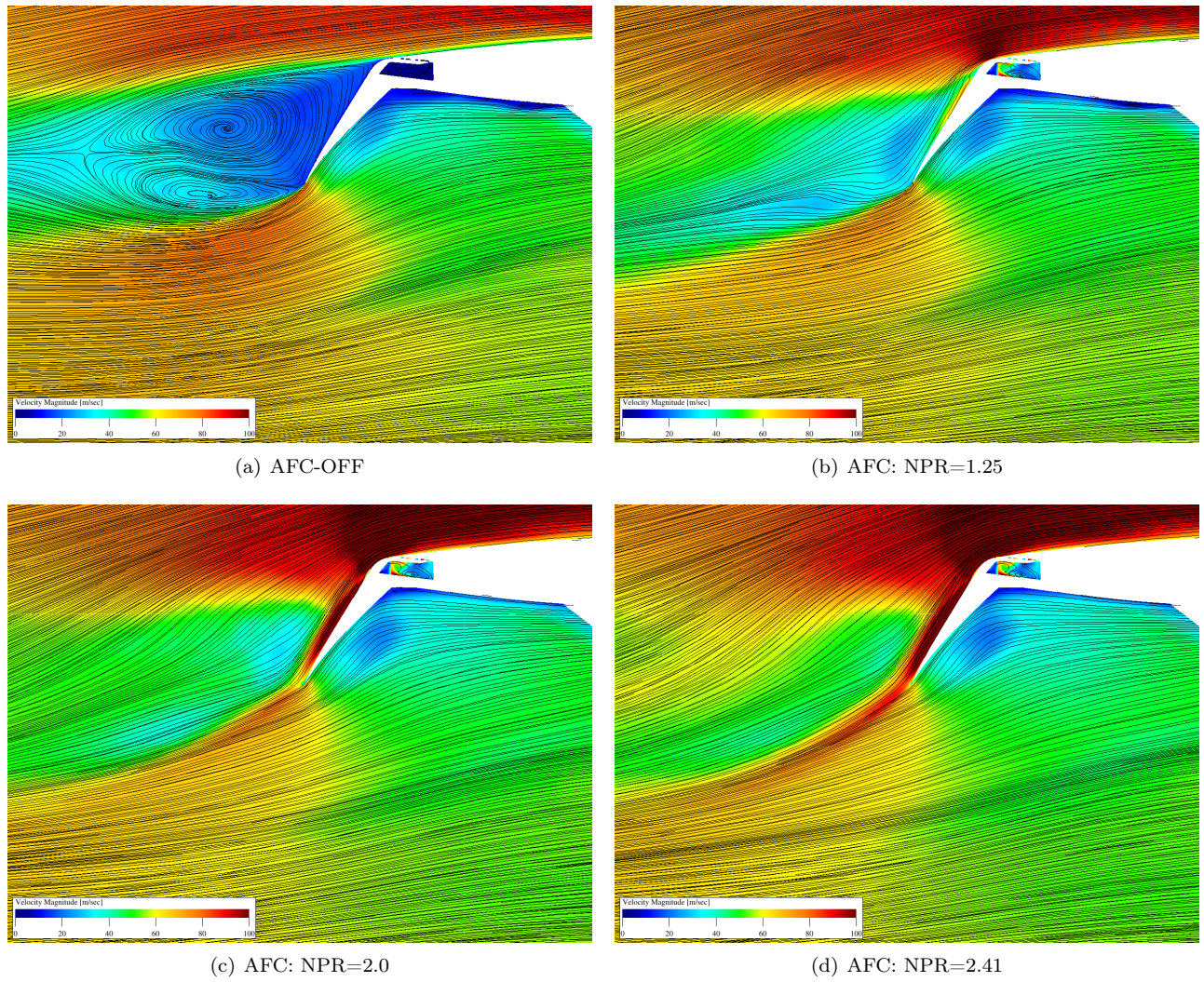
Fig. 21 **Effect of input pressure levels on simulated streamline patterns, y=38.05 inches,** $Mach = 0.2, Re = 3.27 \times 10^6, \alpha = 8°$**.**

(a) AFC-OFF
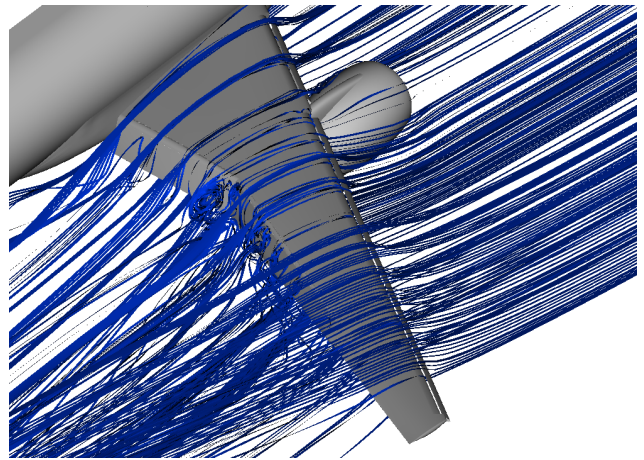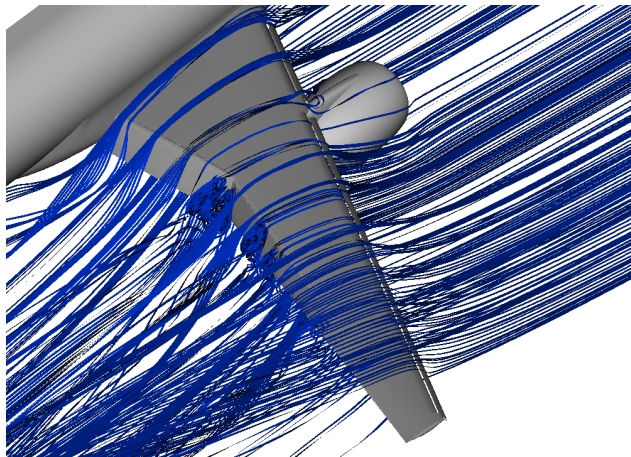
(b) AFC: NPR=1.25

(c) AFC: NPR=2.0

(d) AFC: NPR=2.41

Fig. 22 **Effect of input pressure levels on simulated streamline patterns, y=63.80 inches,** $Mach = 0.2, Re = 3.27 \times 10^6, \alpha = 8°$**.**
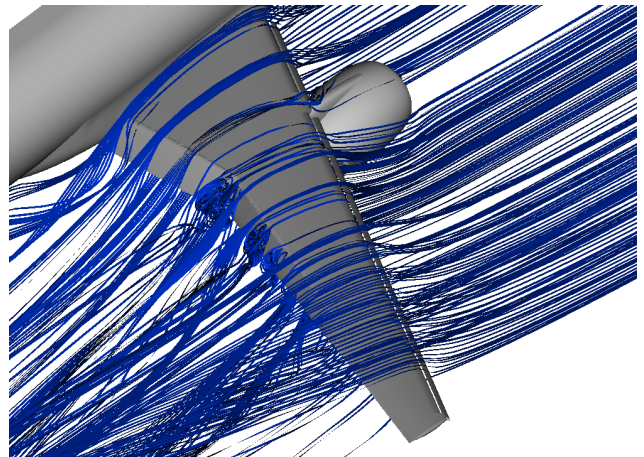
(a) AFC-OFF

(b) AFC: NPR=1.25

(c) AFC: NPR=2.0

(d) AFC: NPR=2.41

Fig. 23 Effect of input pressure levels on simulated 3-D streamline patterns, $Mach = 0.2, Re = 3.27 \times 10^6, \alpha = 8°$**.**